SANDIA REPORT
SAND2022-14255
Printed October 2022

Sandia National Laboratories

High-Speed Diagnostic and Simulation Capabilities for Reacting Hypersonic Reentry Flows: LDRD Final Report

Sean P. Kearney, Elijah R. Jans, Justin L. Wagner, Kyle P. Lynch, Kyle A. Daniel, Charley R. Downing, Darrell J. Armstrong, Ross M. Wagnild, Lawrence Dechant, Jungyeoul Brad Maeng, and Zakari Echo

Prepared by
Sandia National Laboratories
Albuquerque, New Mexico
87185 and Livermore,
California 94550

Issued by Sandia National Laboratories, operated for the United States Department of Energy by National Technology & Engineering Solutions of Sandia, LLC.

Available to DOE and DOE contractors from
U.S. Department of Energy
Office of Scientific and Technical Information
P.O. Box 62
Oak Ridge, TN 37831

Telephone: (865) 576-8401
Facsimile: (865) 576-5728
E-Mail: reports@osti.gov
Online ordering: http://www.osti.gov/scitech

Available to the public from
U.S. Department of Commerce
National Technical Information Service
5301 Shawnee Rd
Alexandria, VA 22312

Telephone: (800) 553-6847
Facsimile: (703) 605-6900
E-Mail: orders@ntis.gov
Online order: https://classic.ntis.gov/help/order-methods/

ABSTRACT

High-enthalpy hypersonic flight represents an application space of significant concern within the current national-security landscape. The hypersonic environment is characterized by high-speed compressible fluid mechanics and complex reacting flow physics, which may present both thermal and chemical nonequilibrium effects. We report on the results of a three-year LDRD effort, funded by the Engineering Sciences Research Foundation (ESRF) investment area, which has been focused on the development and deployment of new high-speed thermochemical diagnostics capabilities for measurements in the high-enthalpy hypersonic environment posed by Sandia's free-piston shock tunnel. The project has additionally sponsored model development efforts, which have added thermal nonequilibrium modeling capabilities to Sandia codes for subsequent design of many of our shock-tunnel experiments. We have cultivated high-speed, chemically specific, laser-diagnostic approaches that are uniquely co-located with Sandia's high-enthalpy hypersonic test facilities. These tools include picosecond and nanosecond coherent anti-Stokes Raman scattering at 100-kHz rates for time-resolved thermometry, including thermal nonequilibrium conditions, and 100-kHz planar laser-induced fluorescence of nitric oxide for chemically specific imaging and velocimetry. Key results from this LDRD project have been documented in a number of journal submissions and conference proceedings, which are cited here. The body of this report is, therefore, concise and summarizes the key results of the project. The reader is directed toward these reference materials and appendices for more detailed discussions of the project results and findings.

ACKNOWLEDGEMENTS

The authors greatly appreciate three years of generous support from the Engineering Sciences Research Foundation. Useful technical exchanges with Mikhail Slipchenko and his students, Austin Webb and Chris Crabtree, at Purdue University, who have been funded on a companion Academic Alliance effort, are also greatly appreciated. We thank Arlee Smith (retired Sandian, currently at AS-Photonics, Albuquerque, NM) for seeding us with the idea of the noncolinear optical parametric oscillator as a Stokes source for high-speed CARS measurements using nanosecond laser pulses. We gratefully acknowledge Daniel Lauriola, Spectral Energies LLC, for his assistance in the construction and setup of picosecond CARS thermometry for our high-temperature shock-tube measurements.

CONTENTS

LIST OF FIGURES

ACRONYMS AND TERMS

Acronym/Term	Definition
CARS	Coherent anti-Stokes Raman scattering
HST	High-temperature shock tunnel or shock tube
PLIF	Planar laser-induced fluorescence
OPO	Optical parametric oscillator
NOPO	Noncolinear optical parametric oscillator
OPG	Optical parametric generator
OPA	Optical parametric amplifier

1. INTRODUCTION

Hypersonic flight systems are a preeminent national-security concern within both DOE and DoD mission spaces. These high-speed, chemically reacting, high-enthalpy environments are characterized by extreme temperatures, uncertain departures from thermochemical equilibrium, and short time scales. Prediction of complex thermochemical phenomena is critical for assessing vehicle performance, heating rates, and signatures and the need for validated, reliable modeling tools is increasingly critical to Sandia's mission space. Existing air- and ablation-chemistry models rely upon mechanisms that have been tuned to limited experimental data, frequently obtained in large-scale, high-enthalpy test facilities, often with poorly quantified flow conditions and limited diagnostic capabilities. Multiple reaction and relaxation rate parameters are tuned in a non-unique way, often to match only a single measured parameter [1, 2].

Space- and time-resolved laser diagnostics for hypersonic flows have not historically achieved the high data-acquisition rates required for application in production ground-test facilities, which are characterized by microsecond- to millisecond-duration test times and high-speed dynamics. Recently introduced burst-mode laser architectures [3, 4] are an enabling technology for high-data-rate diagnostics but have seen only a handful of applications for chemically specific measurements due to complexities in construction of wavelength-tunable burst-mode-pumped sources [5, 6], in particular for wide-bandwidth diagnostic methods such as coherent anti-Stokes Raman scattering (CARS) [7, 8]. In this project, we have cultivated agile solid-state optical parametric gain systems for tunable burst-mode diagnostics, with adjustable spectral bandwidth and repetition rates up to 100 kHz. These sources have been adapted for thermochemical measurements based on laser-induced fluorescence (LIF) imaging and CARS spectroscopy. Nonequilibrium temperatures in N_2, and visualization of NO mole-fraction distribution have been demonstrated in a time-resolved manner, at 100-kHz rates, for measurements in the Sandia free-piston shock-tube and shock-tunnel facilities. We have described these advances in multiple journal submissions and conference papers and briefly summarize the key results in the body of this report. Key reference materials for experimental results include [9-15]:

- E.R. Jans, D.J. Armstrong, A.V. Smith, and S.P. Kearney, "Noncolinear optical parametric oscillator for broadband nanosecond pulse-burst CARS diagnostics in gases," *Optics Letters* **47,** 1839-1842 (2022).
- S.P. Kearney, K.A. Daniel, J.L. Wager, K.P. Lynch, C.R. Downing, D.K. Lauriola, J. Leicht, and M.N. Slipchenko, "Burst-mode coherent anti-Stokes Raman scattering N_2 thermometry in the Sandia free-piston shock tube, AIAA2022-0894, AIAA SciTech Forum, San Diego, CA (2022).
- E.R. Jans, S.P. Kearney, D.J. Armstrong, and A.V. Smith, "Demonstration of a burst-mode pumped noncolinear optical parametric oscillator (NOPO) for broadband CARS diagnostics in gases, "AIAA2022-0896, AIAA SciTech Forum, San Diego, CA (2022).
- S.P. Kearney, D.K. Lauriola, H.U. Stauffer, P. Hsu, N. Jiang, V. Athmanathan, T.R. Meyer, and S. Roy, "Analysis of picosecond coherent anti-Stokes Raman spectra for gas-phase diagnostics, *Journal of the Optical Society of America B* (to be submitted), 2022.
- K.P. Lynch, T.W. Grasser, R.W. Spillers, C.R. Downing, K.A. Daniel, E.R. Jans, S.P. Kearney, B.J. Morreale, R. Wagnild, and J.L. Wagner, "Design and characterization of the Sandia free-piston reflected shock tunnel, *Shock Waves* (accepted) (2022).
- S.P. Kearney, K.P. Lynch, K.A. Daniel, E.R. Jans, C.R. Downing, J.L. Wagner, A.M. Webb, C.Q. Crabtree, and M.N. Slipchenko, "Burst-mode laser-induced fluorescence of nitric oxide

in the Sandia free-piston shock tunnel," AIAA SciTech Forum (accepted), National Harbor, MD (2023). See also SAND2022-7848A.

- E.R. Jans, K.P. Lynch, K.A. Daniel, C.R. Downing, J.L. Wagner, and S.P. Kearney, "Characterization of shock-tunnel free-stream nonequilibrium using nanosecond pulse-burst coherent anti-Stokes Raman scattering, AIAA SciTech Forum (accepted), National Harbor, MD (2023). SAND2022-7970A.

This project additionally has had a significant computational and modeling component. In particular, new species-specific models for vibrational relaxation under thermal nonequilibrium conditions have been developed and inserted into the SIERRA/SPARC Navier-Stokes code. This new modeling capability considers vibrational relaxation for key air-chemistry species, N_2, O_2, and NO, individually, and calculates a unique vibrational temperature for each gas. Prior capability in SPARC considered an effective vibrational temperature for the gas mixture. The details of this new code capability are presented in 0. This new capability has been particularly useful because it has been used to predict nonequilibrium conditions at the exit of the Sandia free-piston shock-tunnel nozzle, which could later be compared to coherent anti-Stokes Raman scattering (CARS) measurements in N_2. The project has additionally supported development of Direct Simulation Monte-Carlo (DSMC) code development for modeling of thermal relaxation in the strong shocks and expansions encountered in hypersonic flight. In particular, a rigorous treatment of detailed balance has been introduced, which applies to relaxation behind shock fronts.

Key reference materials containing computational results include [16] [17] :

- Z. Eckert and M.A. Gallis, "Enforcing detailed balance in the Borgnakke-Larsen redistribution method with temperature-dependent relaxation models, *Physics of Fluids* **34**, 066118 (2022).
- L. Dechant, R. Wagnild, K.P. Lynch, S.P. Kearney, and. J.L. Wagner, AIAA SciTech Forum (accepted), National Harbor, MD (2023). SAND2022-7196C.

2. ENABLING RESEARCH CAPABILITIES AND GOALS

2.1. Sandia Free-Piston Reflected Shock Tunnel and Shock Tube

A primary motivation for this project was to develop diagnostics and simulation tools relevant to high-enthalpy environments in hypersonic flight. At flight enthalpies of ~ 5 MJ/kg or more, these conditions are associated with extremely high temperature, reaching 5000–10,000 K or higher, at km/s gas velocities. These challenging measurement conditions can be reached on the ground in Sandia's recently commissioned free-piston shock-tube and shock tunnel facilities, abbreviated here as HST, or High-temperature Shock Tube/Tunnel. These free-piston facilities, shown in Figure 1, are a core part of Sandia's hypersonic S&T capabilities. A major focus of this LDRD project is development of experimental diagnostics and simulation capabilities to support ground testing efforts in HST.

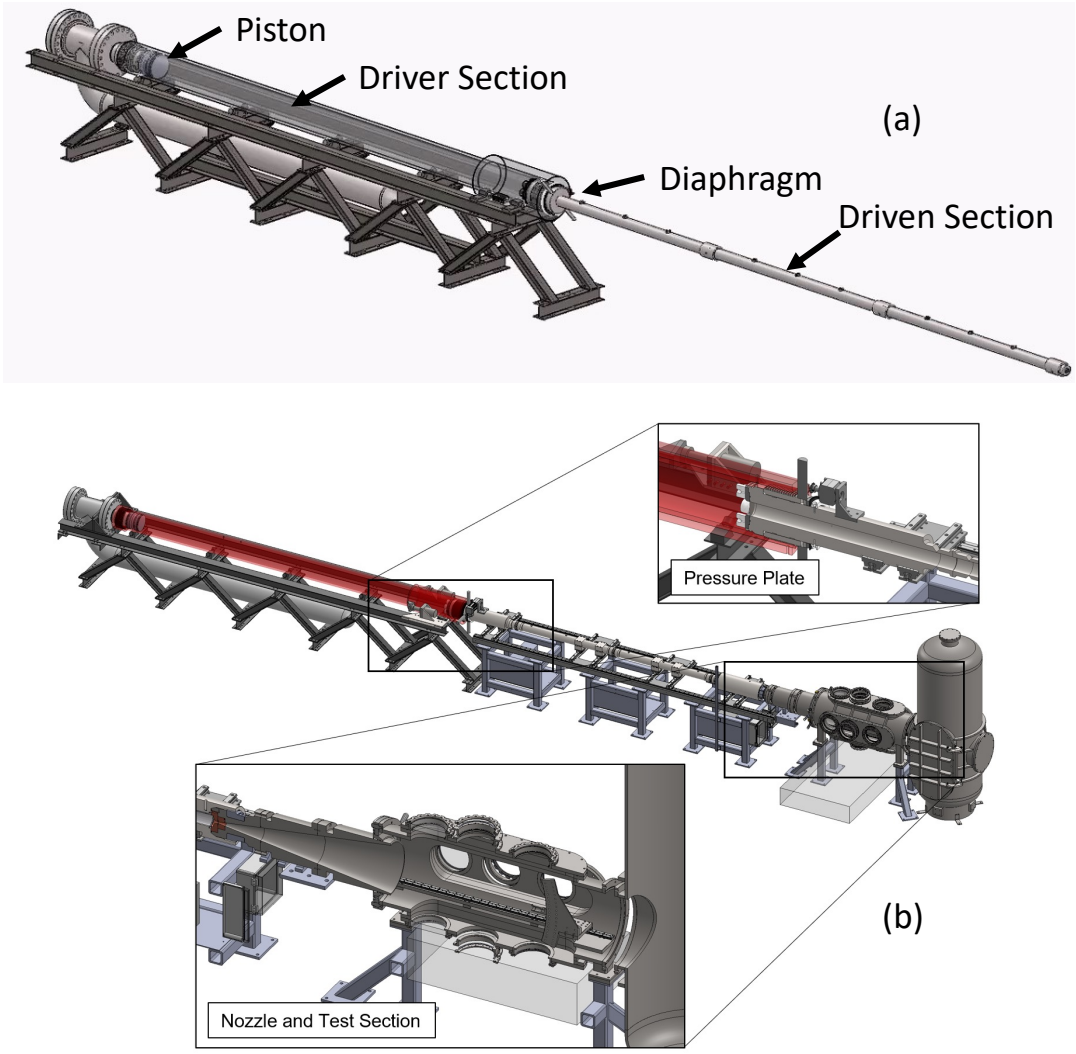

Figure 1 -- Sandia free-piston facility for hypersonic ground testing: (a) shock-tube configuration; (b) shock-tunnel configuration.

The design of HST is described in detail elsewhere [13] and is briefly summarized here. A reservoir section is filled with N_2 at pressures of 7–28 atm, and is used to launch an 11.9-kg piston at speeds approaching 180 m/s down the shock tube's driver section to compress the driver gas to very high temperatures and pressures. Driver gas composition is typically a He/Ar mix, while the driven test gas is typically air or N_2. The driver-gas section has a length of 5.2 m, an inner diameter of 0.267 m, and is separated from the driven test-gas section test gas by a steel diaphragm. The same driver section and piston are used in both the shock-tube and shock tunnel configurations, with the key differences being in the driven section design.

In shock-tube configuration, Figure 1(a), the driven section is composed of four modular tubes, with a total length of 9.2 m, and an inner diameter of 0.087 m. The test section is located at the end of the driven gas tube to allow maximum separation between the incident shock wave and the contact surface interface between the test gas and the downstream-propagating driver section gas—thereby maximizing the useful test time. Upon shock reflection from the test-section end wall, a substantial fraction of the work input from the piston is recovered, heating the test gas to temperatures of $T \sim$ 3000–6,000 K. Each shock-tube experiment is characterized by three thermodynamic state conditions in the test gas, shown in Figure 2: State 1 is an unshocked pre-test state at room temperature and low pressure; State 2 is the condition after passage of the incident shock wave through the test section; and State 5 is the highest temperature and pressure condition reached after a second passage of the shock reflected from the test-section end wall. The shock-tube configuration allows experimenters to access extreme temperature conditions in the post-reflected-shock state for periods of several hundred microseconds.

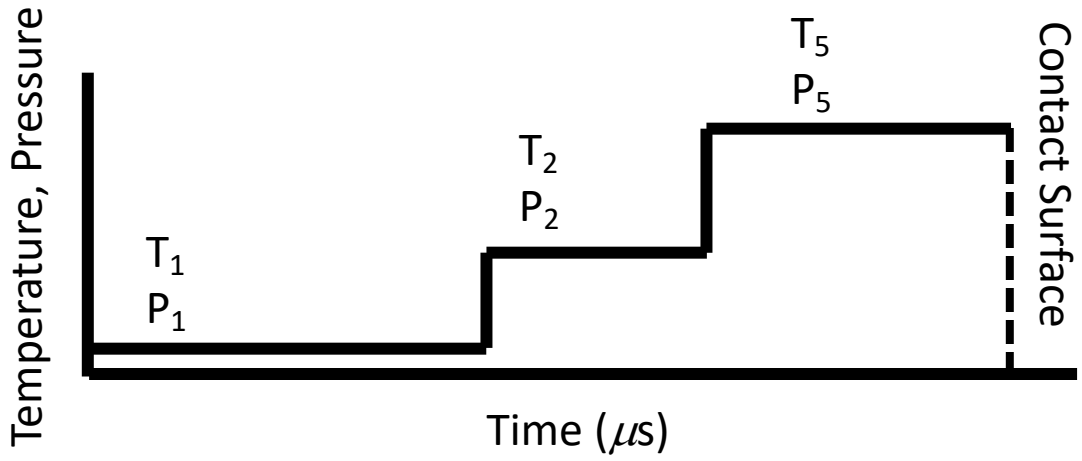

Figure 2 -- Notional drawing of shock tube thermodynamic states. The contact surface represents the arrival of driver gas at the measurement location.

This shock-tube facility can be converted to reflected shock-tunnel mode [13] to achieve flight-relevant velocities (3–4 km/s) and stagnation enthalpy (H = 4-9 MJ/kg) by expanding the high-enthalpy reflected shock-tube gases through a conical supersonic nozzle, shown in Figure 1(b). Upon shock reflection, test conditions in the shock tube section reach temperatures of T = 3000–6000 K

and pressures of P = 80–120 atm, when a helium/argon driver gas mixture is used. A thin foil diaphragm at the throat of the conical nozzle (7.9-deg expansion, 12.7-mm throat, 784 area ratio) breaks, and the high-enthalpy air rapidly expands to freestream conditions in the 0.5-m diameter × 1.4-m long test-section. The free-stream velocity is near 3 km/s at a rotational temperature near T_r = 260 K and a pressure of 2.3 Torr, resulting in a freestream flow near Mach 9. Nonequilibrium effects in the rapid nozzle expansion result in elevated levels of vibrational temperature [18] and a free-stream NO concentration of ~4–5% [14].

2.2. Burst-Mode Laser Capabilities

The burst-mode Nd:YAG laser, illustrated in Figure 3, is a critical enabling technology for the high-speed laser diagnostics demonstrations that are the focus of this project. Gas-phase thermochemical diagnostics have historically relied upon repetitively pulsed laser sources [19], which are limited to repetition rates of ~10 Hz to 1 kHz for commonly employed nanosecond-pulsed Nd:YAG and short-pulse Ti:sapphire lasers. These limitations on repetition rate arise from thermal-management concerns for high-peak-power pulsed laser sources. Burst-mode lasers [4, 20, 21] overcome these thermal limitations by overdriving a Nd:YAG laser gain medium at repetition rates of 10 kHz to as much as 1 MHz, but only for a short, millisecond-duration periods. Heat removal from the laser heads is then achieved during a long dormancy period of about 10 seconds, before another burst of ~100–1,000 pulses can be fired. By operating at such low duty cycle, bursts of high-energy pulses reaching 1J/pulse or more can be achieved with modern burst-mode, or "pulse-burst" laser technology, and these systems are now commercially available.

For chemically specific gas-phase diagnostics, the fixed-wavelength harmonics (1064, 532, 355, and 266 nm) of the Nd:YAG laser must be converted to arbitrarily tunable wavelength values to attain resonance with the gas-phase species to be probed. This is typically accomplished using nonlinear optical crystals inserted into a laser cavity (optical parametric oscillator, OPO) or by direct conversion of short, picosecond burst-mode pulses via optical parametric generation, OPG. A key focus of this project has been the development of tunable burst-mode-pumped sources for thermometry and species measurements, in particular spectrally broad sources for coherent anti-Stokes Raman scattering (CARS) thermometry. These developments are summarized in Section 3.1, with details in [9, 10, 14]

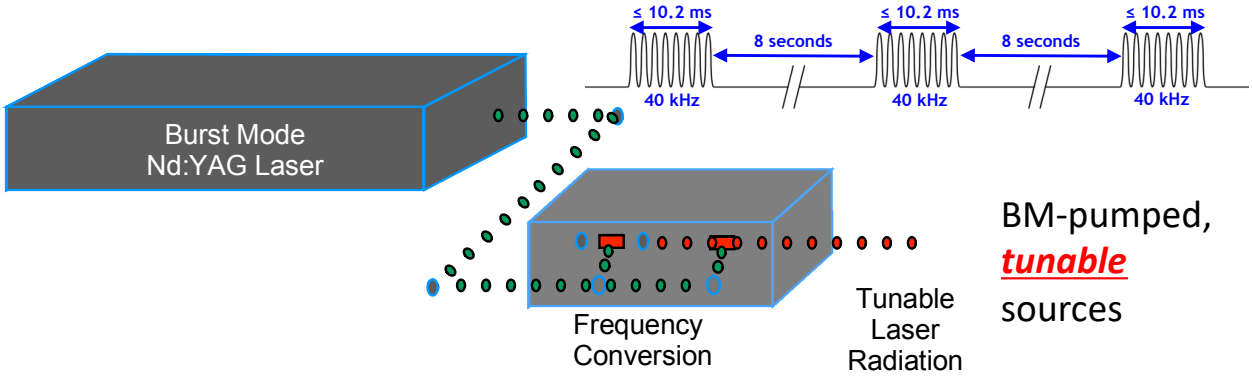

Figure 3 -- Illustration of burst-mode laser concept, including wavelength tunable optical parametric OPO/OPG device.

2.3. Temperature Diagnostic: Coherent Anti-Stokes Raman Scattering (CARS)

Our high-speed temperature measurements were achieved using the CARS diagnostic approach, which has a documented history of robust application in challenging "real-world" test facilities [22-24], where high-temperatures, background luminosity, and particulate that plague many other noninvasive optical approaches can be overcome for successful field measurements. CARS can additionally be utilized for simultaneous measurements of additional parameters, such as species mole fraction [25] and pressure [26]. The method is summarized here in Figure 4. For gas-phase CARS detection, three high-energy pulsed laser beams are crossed at a high-intensity focal spot (Figure 4(a)), which defines a measurement volume that is ~1–3 mm in length and ~50–100 μm in diameter. The CARS process is resonant when the spectral wavenumber (inverse wavelength) difference, $\omega_1 - \omega_S$ is equal to a vibration-rotation Raman transition in the target gas species, as indicated by the energy level diagram in Figure 4(a). This resonant tuning induces a dipole, or "polarization," which scatters the incident probe-laser photons at ω_2 to generate a blue- (anti-Stokes) shifted CARS signal beam at $\omega_{CARS} = (\omega_1 - \omega_S) + \omega_2$. When ω_S is spectrally broadband, a full assembly of transitions can be probed on a single-laser-shot basis, enabling high-speed measurements. The wavelength spectrum of the resulting broadband CARS beam can be fit using theoretical modeling approaches to extract temperature. Calculated high-temperature CARS spectra of N_2 are shown in Figure 4(b). The shape of CARS spectra essentially reflects the thermal vibrational and rotational population distributions in the probed nitrogen gas. At T = 2000 K, two vibrational manifolds are seen, each containing a multitude of rotational transitions that appear as fine-scale "spikes" in the spectrum, whose intensity distribution reflects the width of each vibrational manifold. As temperature increases, the detectable CARS signal appears in an increasing number of vibrational levels, with up to 6 levels observed at T = 6000 K. The width of each manifold increases with the rotational energy distribution.

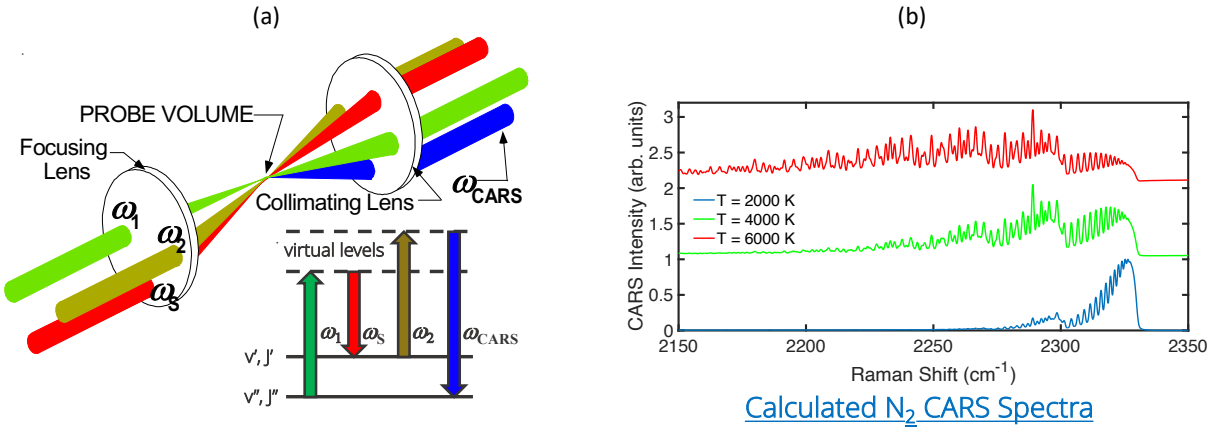

Figure 4 -- Description of CARS technique as a gas-phase temperature diagnostic: (a) CARS laser beam arrangement and energy level diagram; (b) calculated CARS spectra for N_2 gas, illustrating the high-temperature sensitivity of CARS spectra.

Broadband dye-laser sources have historically been used [27] for gas-phase CARS detection with low-repetition-rate pulsed laser sources. Dye lasers present significant barriers for high-speed burst-mode pumping, such as boiling or photobleaching of the dye [28]. Solid-state optical parametric generators

have recently been demonstrated for high-speed CARS thermometry [7, 29]. We pursue similar solid-state solutions in this project.

A key technical achievement for this project has been the application of solid-state broadband, tunable sources for gas-phase CARS. We have demonstrated 100-kHz CARS of N_2 for thermometry using picosecond pulses in the HST shock-tube and nanosecond pulses for improved noise performance in the HST shock tunnel. These advances are summarized in Sections 3.1 and 3.3 and in more detail in references [9, 10].

2.4. Chemically Specific Imaging: Laser-Induced Fluorescence (LIF)

Planar laser-induced fluorescence is a longstanding method for qualitative and quantitative visualization of gas-phase chemical species in flames [30] and in high-speed fluid mechanics [31, 32]. The method is most often deployed for planar imaging by spreading the output of a wavelength tunable source into a sheet of light. When tuned onto resonance, selected species within the light sheet absorb laser photons and re-emit a fluorescence signal, which can be imaged with a gated, intensified camera. As seen at left in Figure 5, laser excitation promotes ground-state (1) molecular or atomic species to excited states (2) by absorption of a single or multiple laser photons at rate B_{12}. Fluorescence emission at rate A_{23} occurs with the decay of the excited-state electron to lower energy level (3). The fluorescence emission is proportional to the concentration of the species to be measured. Quantitative concentration data can be obtained with appropriate corrections for collisional energy transfer (rates Q_{21}, Q_{23}), which provide nonradiative energy transfer and deplete the fluorescence signal yield. The method generally requires ultraviolet laser excitation to access resonant absorption transitions for most species of interest. As shown at right in Figure 5, planar LIF (PLIF) can deliver 2-D imaging capability [31], in this case the distribution of the OH radical is a scramjet combustor.

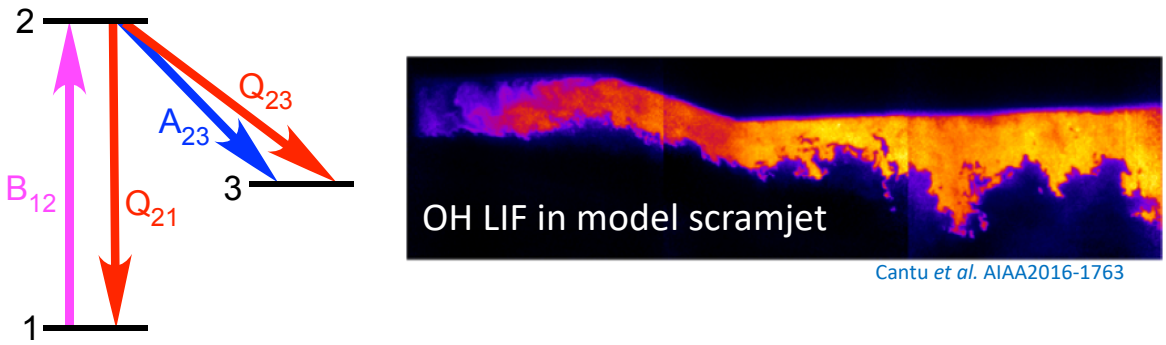

Figure 5 – (left) energy level diagram illustrating laser-induced fluorescence processes for a three-level system; (right) sample planar visualization of the OH molecule in a combustor [31].

2.5. Research Goals

The following research goals were the focus of this R&D:

- Extend our laser-diagnostics capabilities for thermochemical detection from a maximum acquisition rate of 1 kHz to 100 kHz or higher. This 100× speed increase will enable us to time resolve events within HST hypersonic ground tests and increase the total data yield per shot.
- Develop burst-mode-pumped optical parametric conversion schemes to generate high-speed, 100-kHz, tunable puled laser sources. Wavelength tunability is critical to target molecular and atomic resonances needed for species-specific thermochemical diagnostics
- Demonstrate gas-phase thermometry of the N_2 molecule in HST using the coherent anti-Stokes Raman scattering (CARS) technique
- Demonstrate planar imaging of the NO molecule, a critical species for high-temperature air-chemistry, using laser-induced fluorescence.
- Demonstrate a capability to quantify free-stream boundary conditions in HST shock-tunnel experiments; in particular, the free-stream velocity and degree of vibrational non-equilibrium.

3. SUMMARY OF TECHNICAL ACCOMPLISHMENTS

3.1. Burst-Mode-Pumped, Tunable Laser Sources

The CARS and LIF methods discussed above in Sections 2.3 and 2.4 both require tunable laser radiation to access Raman (CARS) and electronic absorption (LIF) resonances. Experimentally, a key goal for this project has been development of robust, wavelength-tunable laser sources, which can be pumped at high speeds by the burst-mode laser. At low repetition rates, tunability has been accomplished using liquid dyes or, more recently, solid-state materials. Dye-laser sources are robust and are readily operated as spectrally narrow (LIF) or broadband (CARS) sources for diagnostics. For high-repetition-rate, burst-mode pumping at 100-kHz or more, dye-laser sources suffer from thermal management issues and photobleaching of dye molecules that have been repetitively pumped by multiple high-energy laser pulses [28]. Solid-state sources employing nonlinear optical crystals do not exhibit photobleaching effects, and are survivable (with limitations) at pump repetition rates into the low MHz range [4].

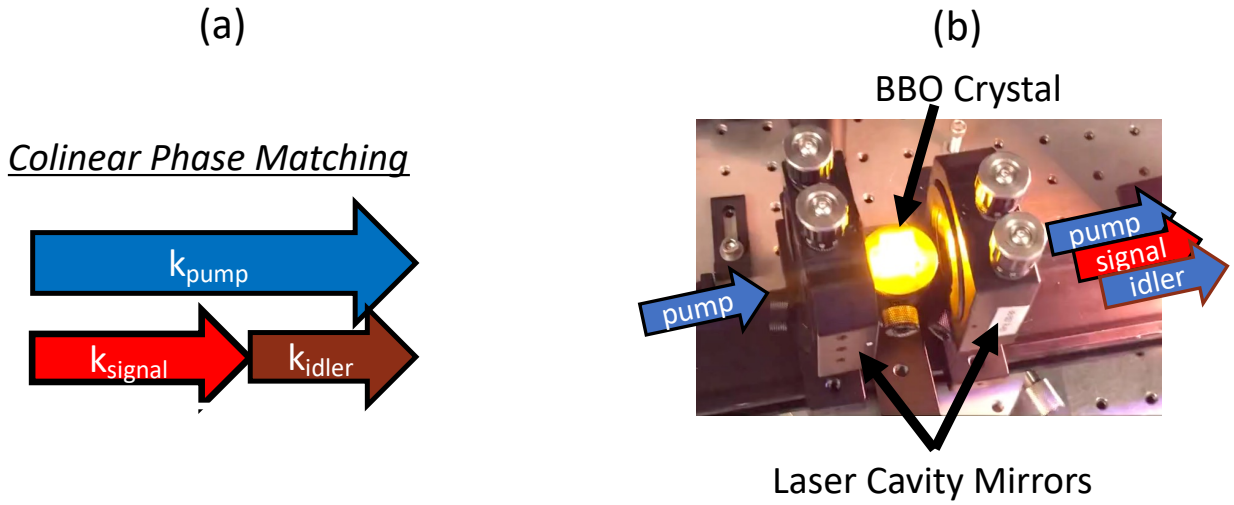

Figure 6 -- Simple colinear OPO construction: (a) wave-vector phase matching diagram per Eq. 2; (b) digital photograph of a simple OPO, with a 355-nm pump beam introduced through the rear cavity mirror. Output pulses emerge colinearly along the laser-cavity axis.

We have cultivated multiple tunable solid-state sources for diagnostics applications over the course of this project; each of these is based on the *parametric down conversion* principle. These optical parametric processes convert a single pump photon into two lower energy (red-shifted) photons termed "signal" and "idler", where the signal is defined as the lowest wavelength (highest energy) of the two generated beams. Photon energy and momentum are conserved in the parametric processes according to,

$$\omega_p = \omega_s + \omega_i \quad \text{and} \tag{1}$$

$$\boldsymbol{k_p} = \boldsymbol{k_s} + \boldsymbol{k_i} \quad , \tag{2}$$

where ω is the photon wavenumber, $\omega = 1/\lambda$, where λ is the wavelength, which is typically expressed in units of cm^{-1}. The wave-vectors, $|\boldsymbol{k}| = 2\pi/\lambda$, are in the direction of laser-beam propagation. Subscipts *p, s,* and *i* reference the pump, signal, and idler photons, respectively. Experimentally, 355-nm third-harmonic photons from the burst-mode Nd:YAG laser pump birefringent, nonlinear optical crystals, typically β barium-borate or BBO. The angle between the crystal axis and the pump beam propagation determines which combinations of photons satisfy Eqs. 1 and 2 and, therefore, the center frequency and bandwidth of the tunable laser source. Wavelength tunability is achieved by rotating the crystal angle.

For our LIF measurements, we constructed a simple optical parametric oscillator (OPO), similar to the one shown in Figure 6. Here, the BBO crystal is placed inside a laser cavity, where the oscillation increases gain, or conversion to signal and idler. The pump, signal, and idler photons are all colinear to the laser cavity axis, which maximizes gain and generally results in narrow spectral widths for long, high-gain OPO crystals. For probing nitric-oxide, the ~621-nm signal light is mixed in a second BBO crystal to yield 226-nm radiation. More details are given in Section 3.4 and in [14].

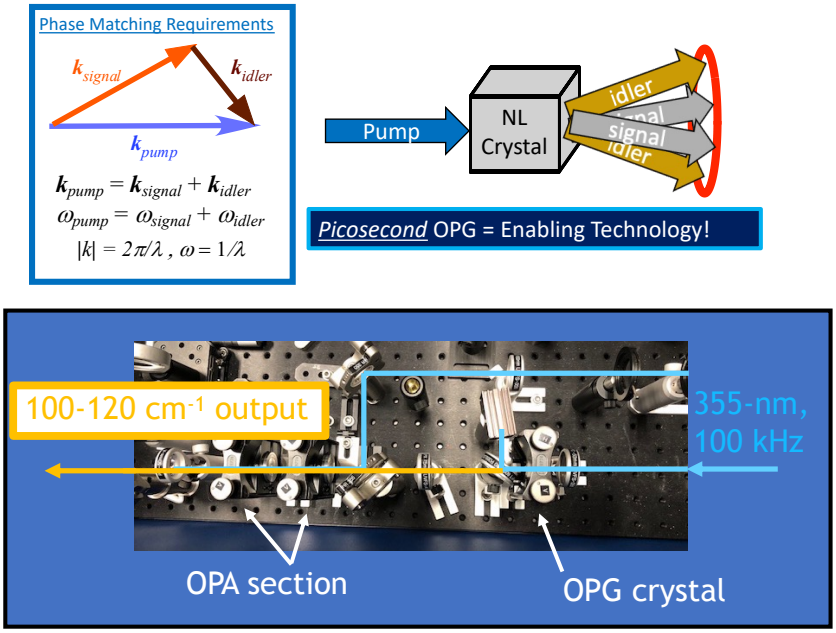

Figure 7 -- Optical parametric generation process (top) and digital photograph of OPA/OPG setup used for 100-kHz picosecond CARS (bottom).

Two different parametric down-conversion schemes were utilized for CARS measurements of N_2. These differ with respect to the LIF OPO because significant spectral bandwidths, in excess of 100 cm^{-1}, are required for single-shot CARS detection. In our first application, summarized in Section 3.2 and in [10], our burst-mode laser was converted from 10-ns duration pulses to ~60-ps pulses. This over 100× reduction in pulse duration yields very high peak powers—intense enough to generate significant conversion to signal and idler without using a laser cavity. When the gain is no longer restricted to the cavity axis, phase matching (Eq. 2) is achieved over much wider spectral bandwidths via *optical parametric generation* (OPG), illustrated here in Figure 7. A single BBO crystal is pumped at

100-kHz generating a "cone" of bandwidth per the graphical representation shown at top right in Figure 7. This simple OPG scheme was used to seed two additional BBO crystals in colinear amplifier stages (*optical parametric amplification,* OPA) and the resulting OPG/OPA setup was deployed as a CARS Stokes source for 100-kHz thermometry in the HST shock-tube configuration.

As discussed below in Section 3.3, we improved our N_2 CARS thermometry results by returning to nanosecond-duration laser pulses. The reduction in peak energy associated with longer pulses required us to reintroduce the laser cavity mirrors, where OPO output bandwidth is typically limited. High-bandwidth, wavelength-tunable nanosecond pulses were generated using a *noncolinear* OPO (NOPO) configuration, where the 355-nm pump beam is introduced at an angle to the laser cavity axis, shown at left in Figure 8. The colinear phase-matching constraint in Figure 6 is relaxed and several hundred wavenumbers of optical bandwidth are observed in the nanonsecond signal output. A comparison of output spectra from 355-nm pumped BBO OPOs in colinear and NOPO configuration is shown in the middle and right-hand panels in Figure 8. The center wavelength of these spectra is tuned near 607 nm, required for CARS probing of N_2, and to 590 nm, required for O_2 CARS. The significant increase in bandwidth from ~5–10 cm^{-1} to 360–430 cm^{-1} enables wideband CARS detection with reduced measurement uncertainty, with details available in [9].

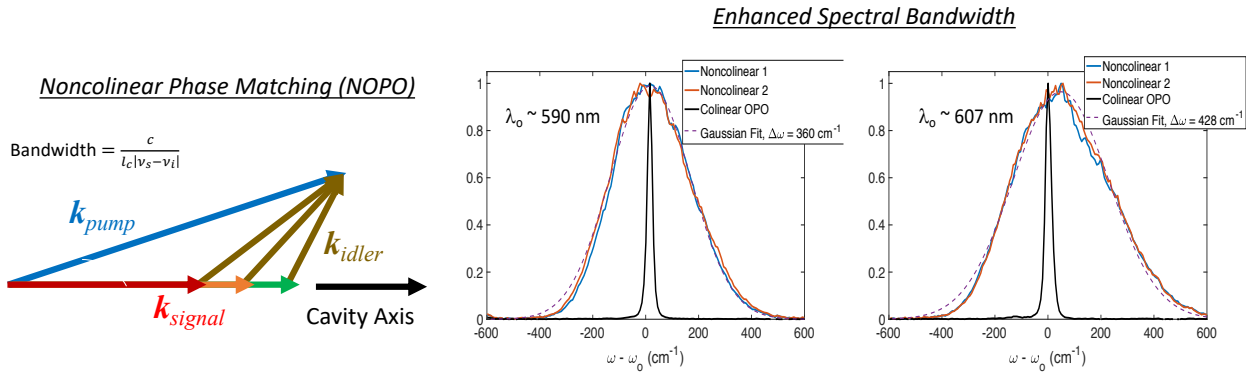

Figure 8 -- Noncolinear phase-matching scheme for broadband NOPO operation (left); observed spectral bandwidth for colinear and NOPO sources (middle, right).

3.2. 100-kHz Thermometry in the HST Shock Tunnel: Picosecond N_2 CARS

Our first demonstration of high-speed laser-diagnostics was undertaken in HST shock-tunnel mode, where temperature conditions in states 1, 2, and 5 of Figure 2 are shown. A key step toward realizing high-temperature thermometry capability was the development of a tunable, spectrally broadband laser source which could be pumped by the burst-mode laser. This was accomplished by taking advantage of the extremely high peak powers afforded by picosecond laser pulses for direct optical parametric generation (OPG) [7, 29] of broadband laser radiation, per Figure 7. Our burst-mode Nd:YAG laser was modified by the manufacturer (Spectral Energies, LLC, Dayton, OH) for generation of short, picosecond laser pulses. Spectral Energies additionally provided us with a custom OPG and optical parametric amplifier (OPA) source for broadband generation, shown in the lower panel of Figure 7. A series of HST shock-tunnel experiments were performed to demonstrate high-temperature thermometry capability using CARS of the N_2 molecule. Representative single-laser-shot

picosecond N_2 CARS spectra are shown in Figure 9(a), where measured CARS spectra are shown alongside best-fit theoretical predictions [12]. Temperature and a factor, α, accounting for the nonresonant contribution to the CARS spectrum were varied as fit parameters. The 100-kHz temperature measurements, shown in Figure 9 (b) can be compared against the expected shock-tube temperatures, calculated from thermodynamic equilibrium, and shown as dashed lines in Figure 9(b).

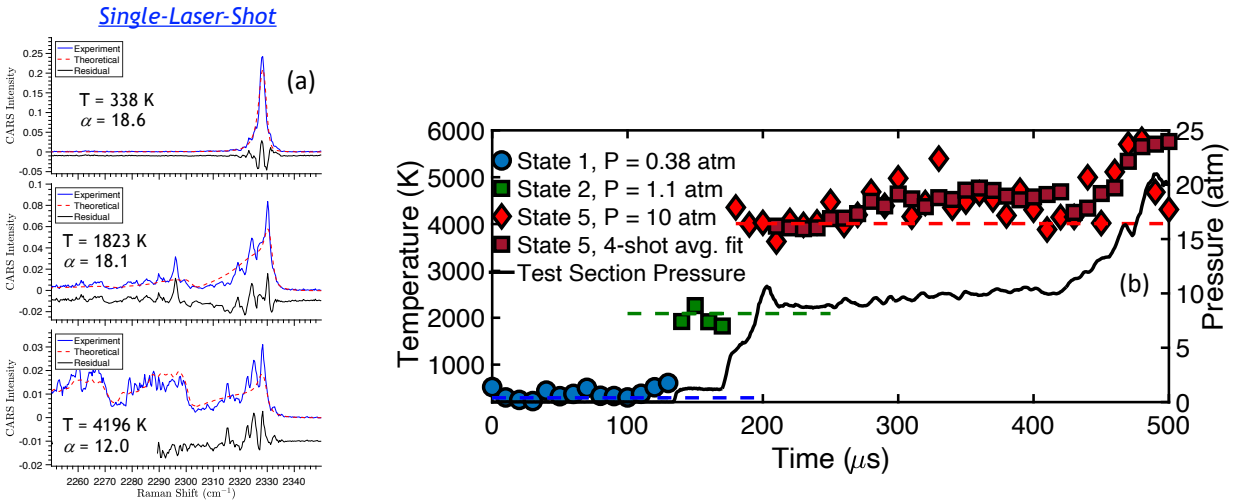

Figure 9 -- Representative picosecond CARS spectra, with fits to a picosecond CARS theoretical model, and resulting 100-kHz temperature measurements for an experiment in the HST shock-tube configuration.

The high-temperature CARS data at T_2 = 2090 K and T_5 = 4013 K are within 5.5% and 11.8% of these equilibrium values, demonstrating the viability of the picosecond pulse-burst CARS technique. In state 5, the initial temperature measurements just after reflected shock passage are in good agreement with equilibrium values. State-5 temperatures continue to rise as the test-section pressure, plotted as a black line, also rises. The large rise in temperature to $T \sim 6000$ K would not be consistent with an adiabatic compression to the measured test station pressures, so we call these late-time measurements into question. The scatter in these temperature measurements is additionally observed to be high. This is a result of the chaotic nature of broadband laser pulses, which necessarily operate far from the Fourier transform limit. The resulting levels of noise in the measured picosecond CARS spectra can be seen in Figure 9(a). We later developed longer, nanosecond-pulsed, broadband sources, which mitigate this noise issue by averaging the CARS process for ~100× longer time, as will be summarized here in Section 3.3.

These picosecond CARS temperature measurements are discussed in more detail in [10]. An enabling technical achievement toward these high-speed temperature measurements is the development of a rigorous theoretical model for picosecond CARS spectra. Previous work [33, 34] has applied long-

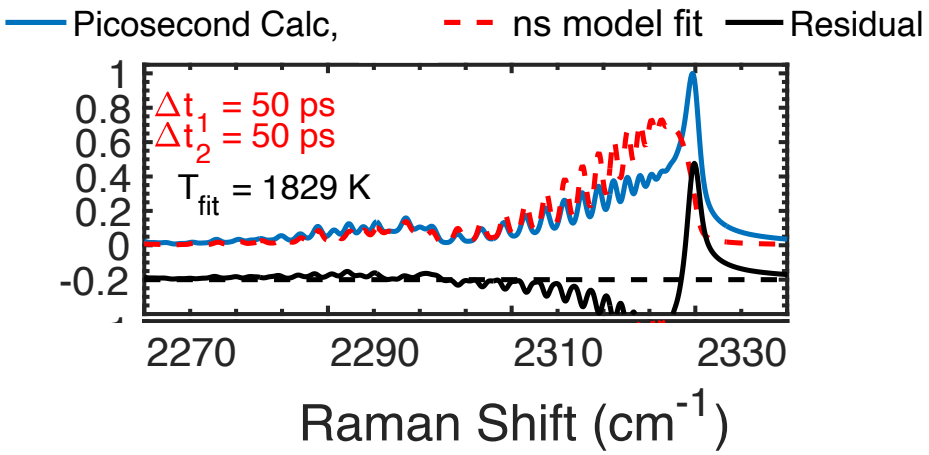

Figure 10 -- Calculated picosecond N_2 CARS spectrum at T = 2000 K and the associated best-fit to a nanosecond CARS model. The picosecond model uses 50-ps laser pulses at zero relative delay, representative of our burst-mode laser system

pulse (nanosecond) theory to these short-pulse measurements, which is shown to be inadequate for the conditions of our measurements. This model was developed at Sandia, with details to be published in [12]. We present a calculated picosecond N_2 CARS spectrum at T = 2000 K, for laser-pulse durations and pulse delays representative of our experiments in Figure 10. A best-fit to a nanosecond CARS model is also shown in the Figure, with a fit temperature of 1829 K—a model-form error of 9.3%. The newly developed, rigorous picosecond CARS model significantly reduces systematic error in these measurements.

3.3. Improved 100-kHz Thermometry: Nanosecond N_2 CARS

While largely successful, our first demonstration of 100-kHz thermometry exhibited higher levels of single-laser-shot noise than is desirable. As discussed in Section 2.3, implementation of a spectrally broad, tunable source is critical for high-temperature single-laser-shot CARS applications. In Section 3.2, this was accomplished by converting our burst-mode system to high-peak-power picosecond pulses, which enabled direct optical parametric generation. The resulting ~100-cm^{-1} bandwidth, ~60-ps duration laser pulses are on the duration of the molecular time scales of the CARS process, which does not allow for sufficient averaging of the noisy broadband laser pulses.

A second broadband solid-state solution, utilizing longer ~10-ns laser pulses, was pursued to reduce CARS measurement noise. The lower peak powers associated with nanosecond pulses required us to place the nonlinear BBO crystal gain medium inside a laser cavity. Operation of an OPO with cavity mirrors typically restricts the tunable output to narrow spectral bandwidths, which would otherwise prohibit single-laser-shot CARS thermometry. This problem was address by tilting the burst-mode pump laser beam with respect to the laser cavity mirrors, thereby operating the OPO in a noncolinear arrangement that can support several hundred cm^{-1} of spectral width, as described previously in Section 3.1 and illustrated in Figure 8. This noncolinear OPO, or NOPO, was applied for improved N_2 CARS thermometry.

A comparison of single-laser-shot temperature measurements performed with picosecond and nanosecond burst-mode CARS is shown in Figure 11. The measurements were obtained in the product gases of near-adiabatic H_2/air flames, where the temperature is steady and well-known. The width of the single-shot temperature data histograms, quantified by the standard deviation, reflects the precision of the temperature measurements. Picosecond pulses yield a standard deviation that is 9.2% of the mean temperature of 2160 K. The precision is improved to 4.9% when nanosecond pulses are employed. Typical best-case measurement precision with repetitively pulsed 10-Hz nanosecond CARS laser pulses is ~3% of the mean at flame temperatures. This high-precision result is obtained with long, 20–30 cm, dye-laser cavities with closely packed longitudinal modes. Our NOPO system has a ~8-cm cavity length, which was kept short to maximize parametric gain. The resulting wider longitudinal mode spacing results in increased single-laser-shot CARS noise. Construction of long NOPO cavities with additional noncolinear parametric amplifier stages is a topic of current research.

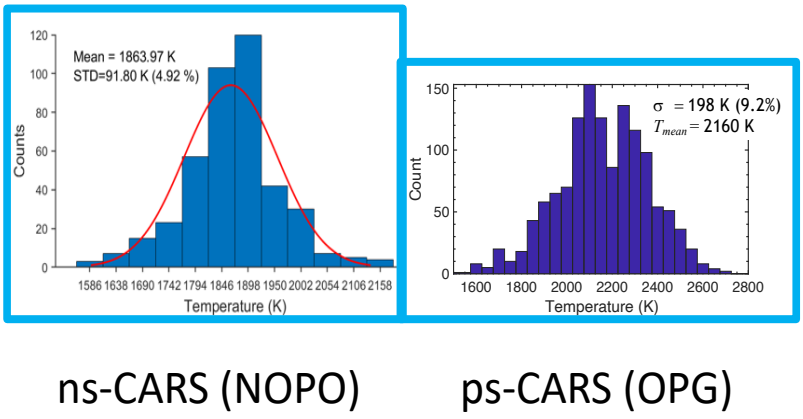

Figure 11 -- Histograms of single-laser-shot temperature measurements performed using nanosecond (left) and picosecond (right) burst-mode CARS in the constant-temperature product gases of H_2/air flames.

The NOPO-based burst-mode CARS instrument was next applied for temperature measurements in the free-stream of a 5-MJ/kg flow in the HST shock-tunnel configuration. Under these conditions, rapid expansion though the shock-tunnel nozzle from a high-temperature, T = 3600-K, stagnation state to a low-density, Mach-9 condition can result in significant thermal (and chemical) nonequilibrium. A SIERRA/SPARC simulation of the shock-tunnel nozzle flow, ***using multi-species vibrational relaxation models supported by this project and described in 0***, is shown in Figure 12. The flow rapidly expands in the nozzle divergence, where the temperature of the rotational and translational degrees of freedom drops to T_r = 260 K, as sufficient molecular collisions are experienced to equilibrate these internal energy modes. Vibrational energy exchange requires several orders of magnitude more collisions, which do not accumulate during the nozzle transit time once the gas density drops in the nozzle divergence. Vibrational temperatures are shown for N_2, O_2, and NO in Figure 12. N_2 displays the slowest vibrational relaxation effect, with T_v remaining elevated at ~2350 K at the exit of the nozzle and into the shock-tunnel free stream. This type of thermal nonequilibrium represents a significant source of uncertainty in the free-stream boundary condition, which can be accounted for with high-speed CARS measurements.

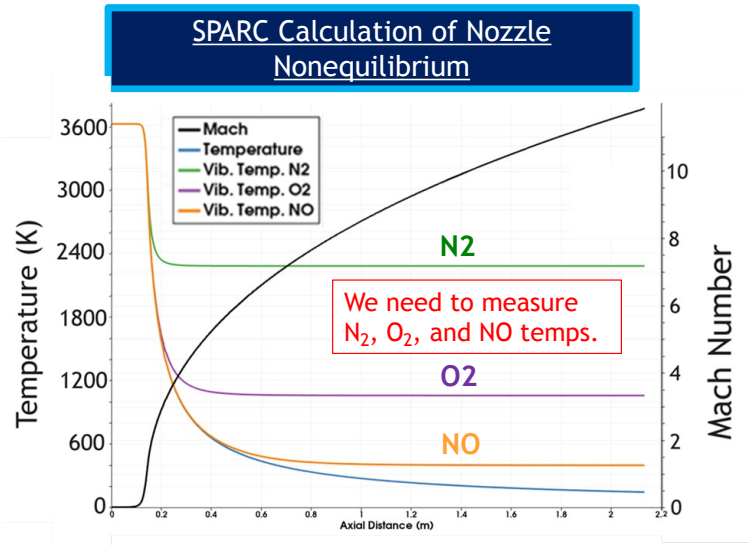

Figure 12 -- SIERRA/SPARC simulation of HST shock-tunnel nozzle flow. The profiles of Mach number, rotational temperature and vibrational temperatures of three molecular species are shown as profiles along the streamwise axis of the shock-tunnel nozzle.

The impact of this degree of thermal nonequilibrium on calculated N_2 CARS spectra is illustrated in Figure 13. The equilibrium condition of $T_r = T_v = 2650$ K is reflected Figure 13(b), which can readily be contrasted with the spectrum calculated at the SPARC-predicted nonequilibrium condition, $T_r = 260$ K, $T_v = 2650$ K in Figure 13(a). The drop in rotational temperature results in a significant narrowing of the vibrational manifolds, where signal from three different populated vibrational levels can be seen at the elevated level of T_v. If an equilibrium condition were attained at $T = 260$ K, then only a single vibrational peak near 2330 cm^{-1} would be present. In this manner, N_2 CARS spectra are exquisitely sensitive to thermal nonequilibrium. A measured single-laser-shot spectrum, acquired at 100-kHz laser repetition rate in the free stream of the 5-MJ/kg shock tunnel flow, is shown in Figure 13(c). The measured spectrum is fit to a two-temperature CARS model and yields an elevated $T_v = 2459$ K at $T_r = 628$ K, consistent with the SPARC prediction of significantly elevated N_2 vibrational excitation. The time-evolution of rotational and vibrational temperatures is shown in Figure 13(d). The dominant ground-state vibrational peak ($v = 0$) near 2330 cm^{-1} was impacted by saturation in some spectra during this measurement campaign, so that only the smaller $v = 1$ and 2 peaks were fit to obtain these nonequilibrium temperature data. A fit to the full spectrum is shown in Figure 13(c) as an example. Free-stream vibrational temperature begins at $T_v = 3200 \pm 250$ K and steadily decays over the 1-ms duration of the experiment, reaching ~2300 K at the end of the test time. Rotational temperature remains low throughout the shot, beginning at ~400–500 K and dropping to ~300 K. Relative uncertainty in the rotational temperature is higher than for the vibrational temperature, but can be improved with enhanced spectral resolution in the measurement. Scatter in the T_v data approaches ±250 K, and can also be improved with above-mentioned elongated NOPO laser cavity. Additional details regarding our NOPO development and nanosecond CARS measurements can be found in references [9] and [18].

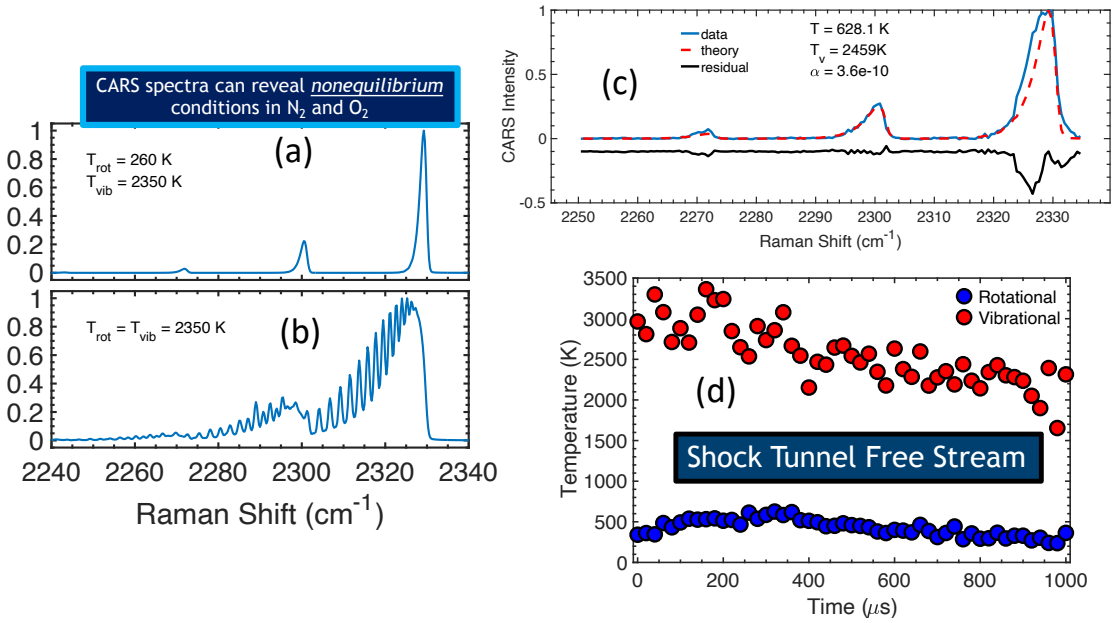

Figure 13 -- Simulated N_2 CARS spectra for (a) predicted nozzle non-equilibrium; (b) thermal equilibrium at T = 2350 K. (c) Representative single-laser-shot CARS spectrum acquired at 100-kHz rate in the shock-tunnel free stream (d) CARS-measured rotational and vibrational temperatures from shock-tunnel free stream.

3.4. High-Speed Visualization of Nitric Oxide in Cylinder Wake Startup Flows

We utilized the planar laser-induced fluorescence (PLIF) technique described above in Section 2.4 for imaging of the nitric-oxide (NO) distribution at 100-kHz rate during startup flow over cylinders in the HST shock-tube and shock-tunnel configurations. For the shock-tube experiment, a 60/40 mole-fraction He/Ar driver gas mixture was compressed to a pressure and temperature of 130 atm and 2200 K, resulting in a 2.9 km/s shock compression of ambient air in the test-gas section, initially at pressure of 4.5 Torr. A 9.5-mm diameter cylinder spanned the test section. Following passage of the incident shock wave, the cylinder wake flow was impulsively started in the induced flow of post-shock air at velocity of ~2.5 km/s, pressure of 0.53 atm, and a temperature near 3000 K. At equilibrium conditions, the NO mole fraction in the shock-heated air approached 4.2%, providing a significant level of fluorescent tracer for PLIF visualization.

The cylinder wake experiment is shown schematically in Figure 14. The 355-nm third harmonic of the burst-mode laser output at 100-kHz repetition rate was used to pump the robust OPO design shown in Figure 14(a). The OPO output wavelength was tuned to 226.05 nm to pump the (0,0) vibrational bandhead, within the NO $A^2\Sigma - X^2\Pi$ system. The nominal bandwidth of the OPO output was ~10–15 cm^{-1} so that a large number of rotational transitions near the bandhead were accessed. The UV laser beam was propagated to the test section and formed into a diverging laser sheet using two cylindrical lenses; sheet height at the beam waist is ~100 mm and the beam waist was placed at the spanwise centerline of the cylinder wake. The NO PLIF signal was collected at right angle to the 226-nm laser sheet with a UV camera lens (Cerco, 100-mm, f/2.8 or Cerco 45-mm, f/1.8, depending on

the required field of view). The resulting NO PLIF images were acquired with a Photron SA-Z high-speed CMOS camera, fitted with a high-speed, lens-coupled, gated image intensifier (LaVision HS-IRO). A 9-mm × 22-mm region in the cylinder wake was imaged, with the 22-mm dimension oriented in the streamwise flow direction.

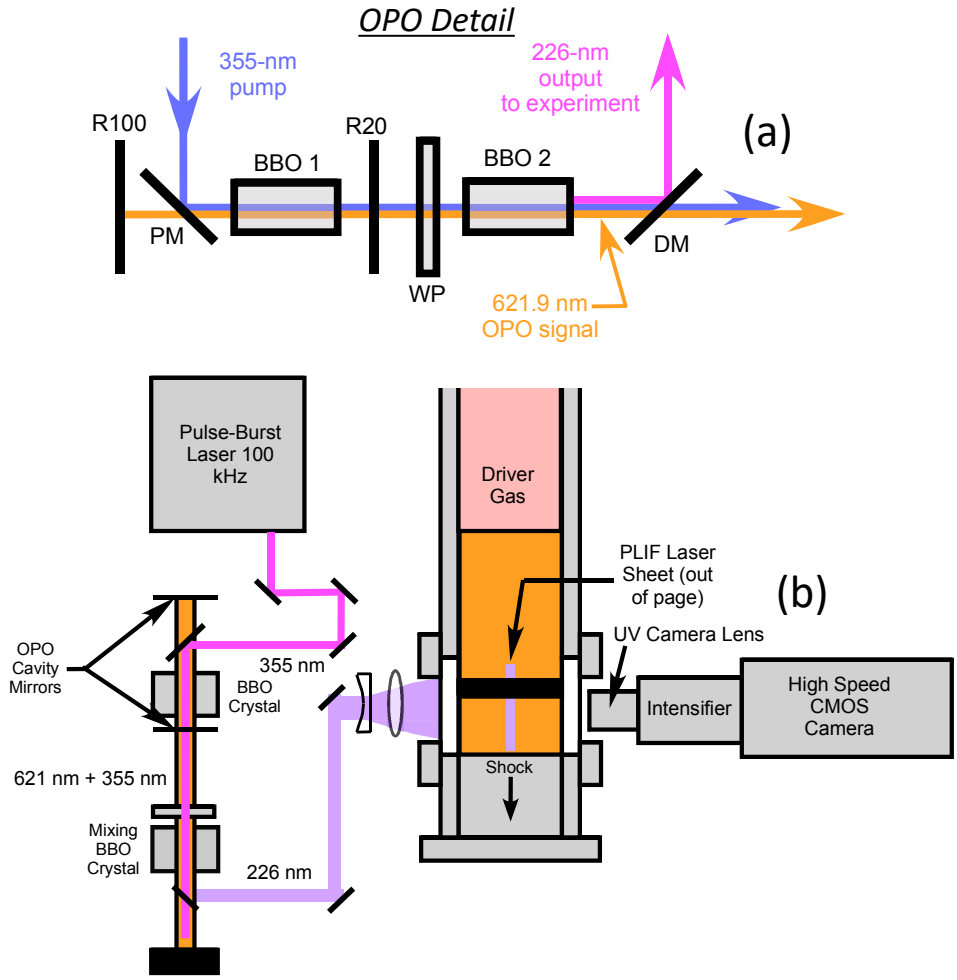

Figure 14 – Details of 100-kHz NO PLIF imaging experiment for cylinder wake flow in the HST shock-tube: (a) detail of tunable burst-mode OPO system used to convert 355-nm burst-mode laser output to 226-nm. (b) experiment schematic.

A sequence of PLIF images which illustrate the cylinder-wake startup flow for the post-shock, U = 2.5 km/s, T = 3000 K free stream in facility shock-tube configuration is shown in Figure 15. In these images, the flow is from left to right, with downstream side of the cylinder at the left-hand side of the images near $x = 0$. The PLIF laser sheet propagates from top to bottom, such that the shadow created by the cylinder can be seen at left-hand side of the images for $t > 3$ μs. The color contours reflect PLIF intensities, corrected for the 226-nm laser sheet profile determined from the PLIF signal in the

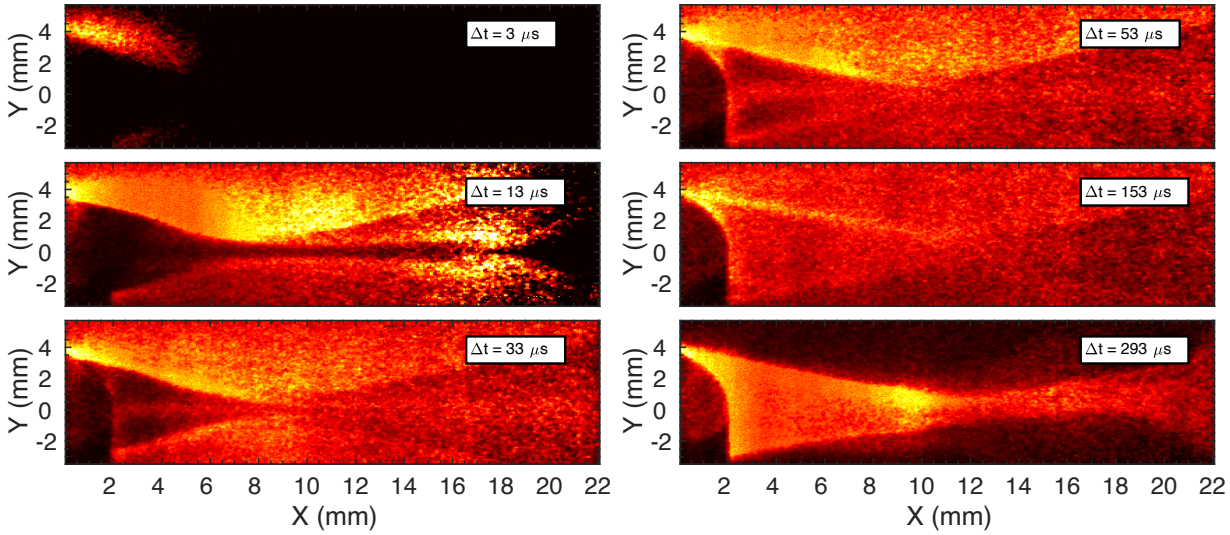

Figure 15 -- Sequence of NO PLIF images acquired during cylinder wake startup flow in the HST shock-tube configuration.

uniform-condition free stream at the top of the images. The incident shock propagates into low-pressure (P = 4.5 Torr) air with zero NO content and NO is formed in the high-temperature, compressed gas behind the shock wave. At time = 3 μs, the incident shock wave has just passed over the cylinder; PLIF signal from post shock NO is observed just above the cylinder for x = 0–6 mm. By t = 13 μs, the shock has propagated to the downstream edge of the field of view. A transient cylinder wake appears. Contrast in the PLIF images is provided by the gradient between an NO concentration deficit in the wake and the NO-rich free-stream flow. The cylinder provides an obstruction for the incident shock wave, such that the initial wake flow is not shock compressed and very little NO PLIF signal is generated there. Two wake vortices, symmetric about the spanwise centerline at y = 0, are visualized in the PLIF images for t = 13–53 μs. At t = 13 μs, the low-pressure, low-NO wake region extends along the full streamwise extent of the imag in a thin region along the y = 0 wake centerline. This long wake starting feature has passed by t = 23 μs. The streamwise extent of the near-field wake grows from ~8 to 11 mm between t = 13 and 53 μs. The downstream edge of this low-pressure wake region is marked by the emergence of a recompression shocks, which appear at ~16-deg to the streamwise axis and are symmetric about y = 0. By t = 153 μs, a steady wake flow has been established. Wake vortices are no longer well visualized, as NO has diffused into the wake, with a corresponding increase in PLIF signal. The low level of contrast in these long-time PLIF images is largely provided by pressure and temperature variation between the free-stream, wake, and recompressed regions of the flow. By t = 293 μs, helium/argon driver gas arrives in the free-stream flow at the test location. A high degree of contrast is observed between the now NO-deficient free stream and the NO-rich, low-speed wake.

The cylinder wake startup flow was simulated using SIERRA/SPARC and the resulting temperature and concentration fields were used as inputs to a first-order model of the PLIF signal amplitude, which includes the effect of the local gas number density and quenching of the PLIF signal by collisions of

NO with itself and other gas partners. The leading order structure of the wake flow PLIF images is captured by the simulations, displayed in Figure 16, including the symmetric wake vortices, long streamwise deficit of NO along the wake centerline, and recompression shock structure. The measured streamwise extent of the wake vortices appears to be longer in the experiment than in the SPARC simulation.

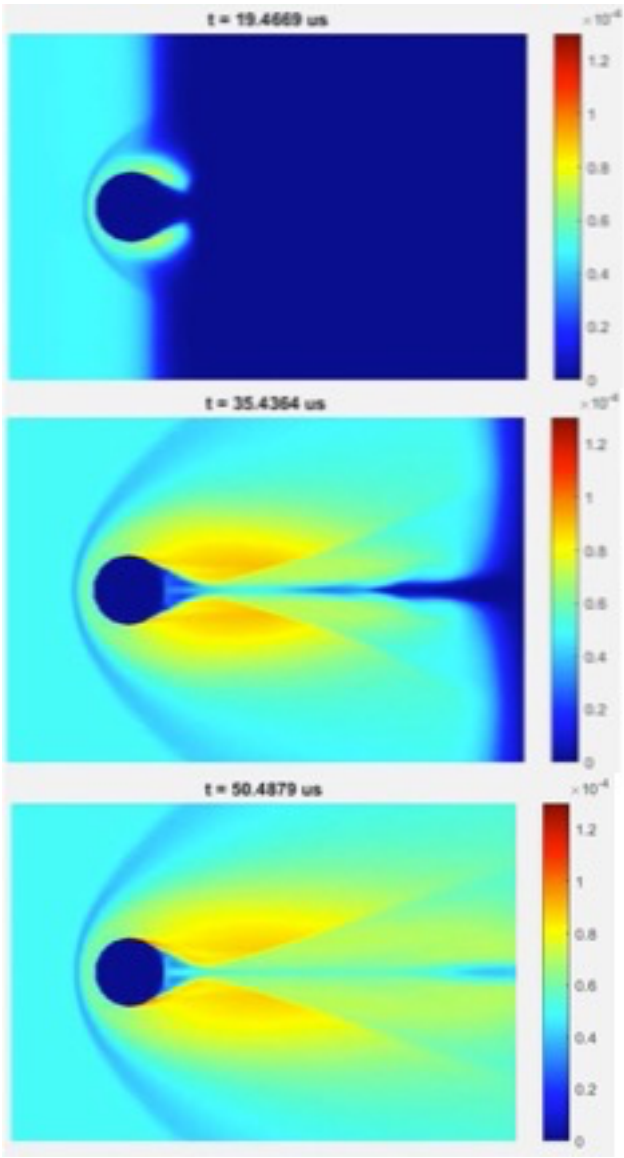

Figure 16 -- Simulated NO PLIF signals for wake startup flow. The colorbar indicates relative PLIF intensities in arbitrary units.

3.5. NO PLIF Visualization and Velocimetry During HST Cylinder Startup Flows

The HST was converted to the shock-tunnel configuration for a second round of 100-kHz NO PLIF imaging experiments. NO PLIF images of the startup and steady-state flow over a 50-mm diameter cylinder in 4.6 MJ/kg, 3 km/s free-stream shock-tunnel flow are displayed in Figure 17. PLIF signal-to-noise is significantly larger in these images than for the cylinder wake shock-tube experiments in Figure 15. An increase in PLIF signal was achieved by removing a filter from the UV camera lens that was used to reject background emission from the shock-tube gases. A 150-ns intensifier gate was sufficient to remove the majority of the hot-gas emission background, with the exception of the stagnation-point region, once the shock tunnel flow reached steady state. In Figure 17, the 3 km/s, $M \sim 9$ flow is from top to bottom and the laser sheet propagates from right to left, with a shadow region observed behind the cylinder on the left-hand side of the images. Transient startup of the shock-tunnel flow is visualized in the images on the left-hand side of Figure 17. At $t = 0$, NO-containing gas has just arrived at the test-section. Significant background emission from NO and, potentially, atomic oxygen is observed near the front stagnation point, and the NO PLIF signal appears in the free stream.

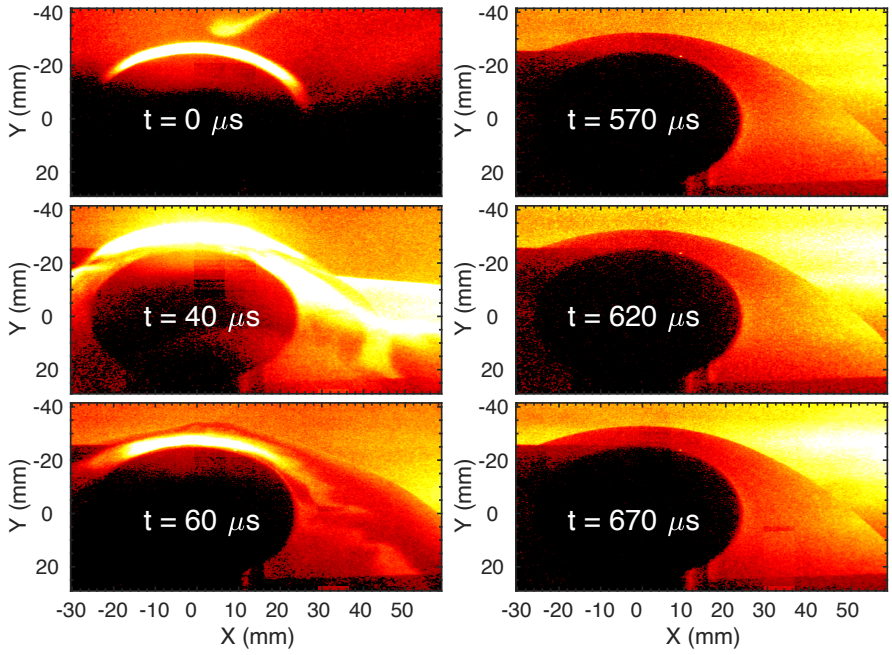

Figure 17 -- Sequence of NO PLIF images acquired during cylinder startup flow in HST reflected-shock-tunnel configuration

By $t = 40$ and 60 μs, a strong, still unsteady, bow shock structure is established, with significant background emission persisting in the front-stagnation region of the cylinder. This background emission significantly drops and the flowfield becomes steady during the main facility test time, which lasts 1 ms or more. PLIF images during steady shock-tunnel flow are shown on the right-hand side of Figure 17 for $t = 570$–670 μs. A stationary shock wave is established, with a front standoff distance of 7.6 mm, or $0.15D$. Image contrast across the bow shock structure is provided by a decrease in PLIF signal between the cold, low-pressure freestream and shock-compressed gas near the cylinder. The

decrease in signal across the shock front results from movement of the lower-state population to higher rotational levels with increasing temperature and from increased collisional quenching of the PLIF signal due to increased post-shock density.

NO fluorescence lifetimes in the low-pressure free stream are observed to approach 100 ns, which is sufficiently long to track motion at the km/s free stream speeds expected in the shock-tunnel flow. Quantification of free-stream conditions is important in shock-tunnel experiments because rapid expansion of shock-tube gases to hypersonic speeds can result in non-equilibrium thermodynamic conditions that increase uncertainty in the nozzle exit flow conditions [35]. This rapid expansion resulted in the nonequilibrium thermal conditions, quantified by CARS measurements in Section 3.3. Elevated free-stream NO levels are additionally a byproduct of these nonequilibrium nozzle processes, but the presence of NO provides a nascent tracer for molecular-tagging velocimetry. De Souza *et al.* [36, 37] have recently demonstrated NO velocimetry in their hypersonic facility, using a single-image technique with a low-repetition-rate Nd:YAG-pumped dye laser, where the LIF signal generated at the spherically focused beam waist was exposed on the camera throughout the fluorescence lifetime. An analytical model was used to extract velocity from the width of the resulting "streaked" LIF image.

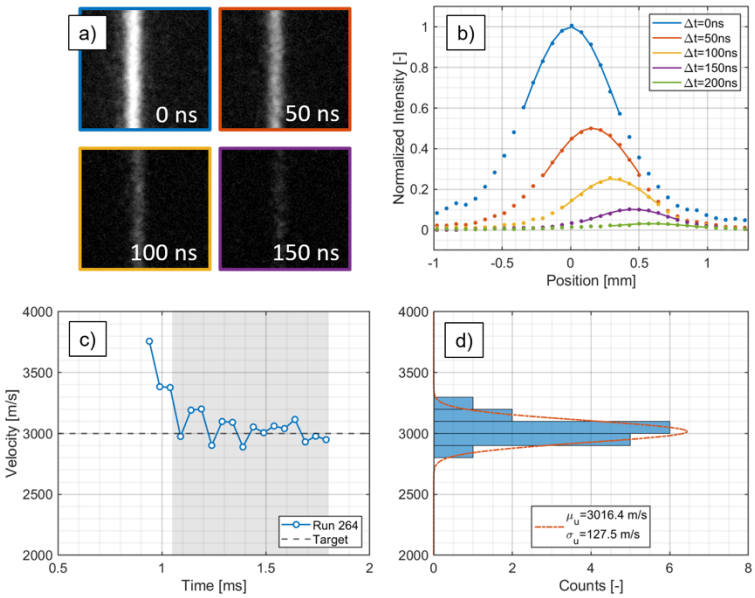

Figure 18 -- Free-stream velocimetry results obtained via molecular tagging of nascent NO in the reflected shock-tunnel: (a) LIF signal intensity in the beam-waist region located in the tunnel free stream; (b) LIF intensity profiles across the width of the beam waist, with fits to the near-peak data shown; (c) time-resolved velocimetry during shock tunnel startup; (d) histogram of velocity measurements during the steady flow test period.

Here, we take advantage of the pulse-burst laser to track fluid motion with a short, 50-ns detector gate, reducing the movement of the LIF emission during camera exposure. The cylindrical sheet-forming lenses used for PLIF visualization are replaced by a single 500-mm singlet lens to focus the 226-nm laser sheet to a well-defined beam waist. Motion of the beam waist is tracked by repetitively sequencing the delay between the burst-mode laser pulses and the intensifier gate from 0 to 200 ns in 50-ns increments. Results from this molecular tagging experiment are shown in Figure 18.

Fluorescence from the beam-waist region in the shock-tunnel free stream is effectively imaged over the long lifetime of the LIF signal. Each of these free-stream LIF lines was processed by first averaging the signal over the beam-waist axis to obtain profiles of LIF intensity across the diameter of the laser beam waist. These intensity profiles were fit to a Gaussian form in the near-peak region, Figure 18(b), to determine peak displacement as a function of time delay. The resulting free-stream velocity data are shown in Figure 18 (c) and (d). These measurements represent the average free-stream speed over 5 consecutive burst-mode laser shots, at a laser repetition rate of 100 kHz—or a 50 μs time resolution in the velocity data. The shock tunnel velocity decays from a maximum of U ~3750 m/s to a steady condition of 3016 m/s ± 127 m/s.

When combined with CARS measurements of free-stream thermal nonequilibrium, the high-speed NO PLIF capability developed here can be used to quantify free-stream velocity and, potentially, NO concentration. Quantification of the impact of free-stream thermochemical nonequilibrium can remove a key source of uncertainty in future code-development and model-validation experiments.

3.6. Advances in SIERRA/SPARC Modeling Capability

The high enthalpy application space associated with a range of hypersonic national security-class problems requires access to advanced computational tools for a predictive design capability. The flow simulation computational suite utilized for this purpose is SIERRA/SPARC (Sandia Parallel Aerodynamics Reentry Code). SPARC is a compressible computational fluid dynamics (CFD) code developed to analyze aerodynamics and aerothermodynamics problems. SPARC solves the Navier–Stokes and Reynolds-Averaged Navier–Stokes (RANS turbulence models) equations on structured and unstructured grids using a cell-centered finite volume discretization scheme. SPARC is equipped with a multiple temperature formulation that partitions

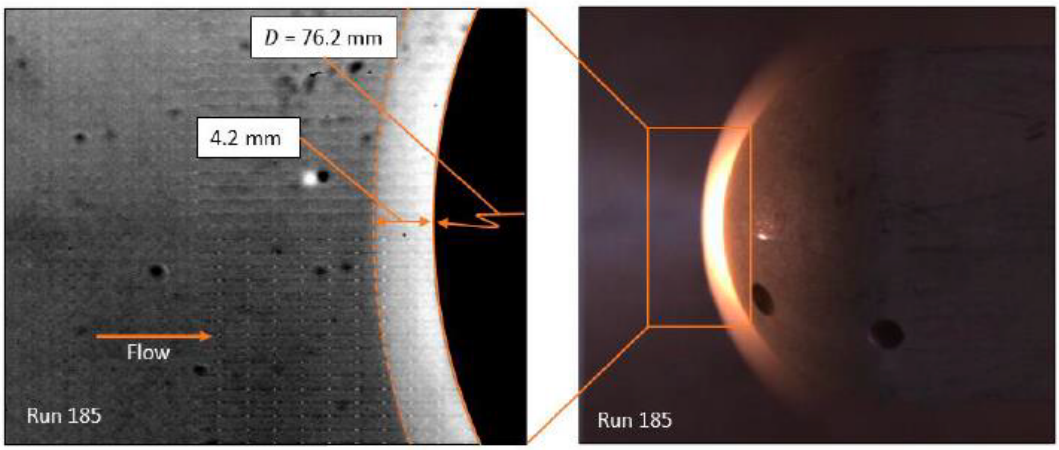

Figure 19 -- Shock-standoff distance measurement in an HST shock-tunnel experiment: (left) schlieren image of the bow shock position in the stagnation region on a cylindrical bluff body; (right) corresponding frame from a color high-speed video with visible radiative emission from the post-shock gases.

temperatures across translational-rotational and vibrational components. The traditional two temperature formulation follows the Park formalism [1, 2], but a more complete version that employs chemical species-specific vibrational energy relaxation is also available and has been added to SIERRA/SPARC with support from this LDRD project. Details of this new multi-species capability can be found in 0. It is examination and validation of the SPARC multi-diatomic species temperature partition formulation that connects high-enthalpy measurement and simplified theoretical arguments to the broad range of computational and experimental programs supported by Sandia.

The relationship between measurements and multi-species relaxation modeling is illustrated by the comparison between shock-tunnel nozzle simulations and CARS measurements of thermal nonequilibrium in Figure 12 and Figure 13. While measurement provides a most essential validation of computational approach effectiveness, a traditional supplement is examination of simplified theory-based efforts. In ref. [17], we describe the shock stand-off distance for blunt forebodies, shown for an HST shock-tunnel experiment in Figure 19, using a simplified differential-equation-based approach with extensions for high enthalpy dissociative chemistry effects. Self-similar differential equations valid for spherical and cylindrical geometries that are modified to focus on the shock curvature induced vorticity in the immediate region of the shock are solved to provide a calorically perfect estimate for shock standoff distance that yields good agreement with classical theory. While useful as a limiting case, strong shock (high enthalpy) calorically perfect gas results required modification to include the effects of dissociative thermo-chemistry. Using a dissociative ideal gas model for dissociative equilibrium behavior combined with shock Hugoniot constraints, we solve to provide thermodynamic modifications to the shock density jump thereby sensitizing the simpler result for high enthalpy effects. The resulting estimates are then compared to high enthalpy stand-off data from literature, recent dedicated high-speed shock tunnel measurements, such as in Figure 19, and multi-temperature partitioned implementation CFD data sets.

Specifically, we examine the high enthalpy thermochemistry models deployed in SPARC, i.e. the more traditional two-temperature vibrational partition model and the diatomic-species-dependent multiple-temperature formulation in 0. A comparison between the vibrationally "frozen" simulation (no relaxation), the two-temperature Park model [1, 2], and the multi-temperature species-dependent model is shown here in Figure 20.

Low-enthalpy/Mach number results for all of the computational models (frozen, two-temperature and multi-temperature) honor the calorically perfect models as one would expect. The two-temperature and multi-temperature results then agree well for high enthalpy/Mach number, where all species tend to vibrationally equilibrate yielding effective two-temperature-like behavior. However, for Mach numbers below $M \sim 8$, individual species vibrational behaviors are important as reflected in the variation in the two standoff distances in Figure 20 for these conditions. Generally, the theoretical results derived here compared adequately with data sources [17], suggesting that the current formulation provides an approximate, but useful, estimate for shock stand-off distance. Further, though analytically convenient, and common for simplified design application, theory-based approaches cannot capture the full physics behavior over a supersonic-hypersonic Mach number span, demonstrating the necessity for species-specific vibrational computational tools.

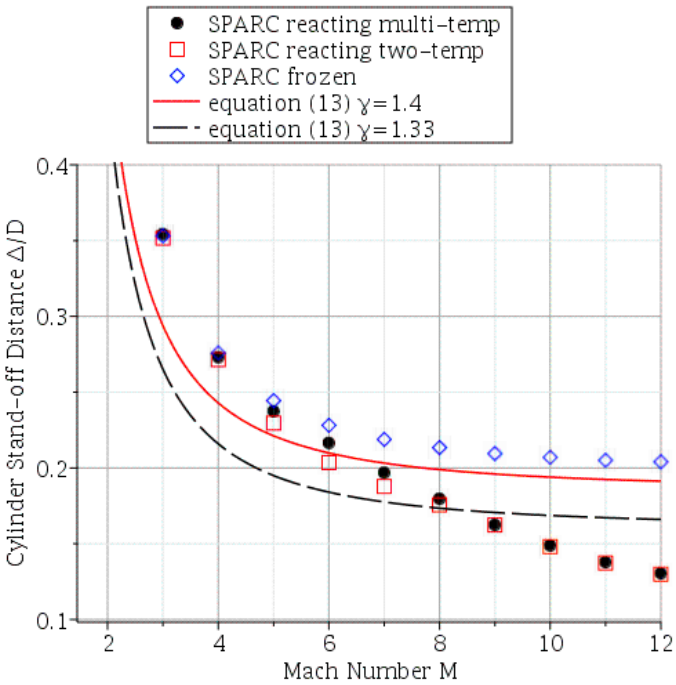

Figure 20 – Comparison of SIERRA/SPARC predictions of stagnation-region shock standoff distances using three different vibrational relaxation models to theoretical predictions presented in ref. [17].

4. SUMMARY AND CONCLUSION

This LDRD-funded work provides Sandia with new diagnostic and simulation capabilities supporting hypersonics S&T. LDRD funding enabled development of high-speed diagnostic tools that enable characterization of extreme-temperature thermochemical environments at flight-relevant conditions, particularly for investigations in the free-piston High-temperature Shock Tube/Tunnel (HST). These high-speed diagnostics capabilities either previously did not exist or did not exist at Sandia. Examples of technical *impact* include:

- Time-resolved quantification of nonequilibrium ground-test facility boundary conditions, including thermal non-equilibrium and its impact on free-stream speed. Uncertainty in test facility boundary conditions is a key impediment to the integration of codes and experiments. New diagnostic capabilities quantify the HST environment.
- Integration of experiments and simulation via new chemically specific formulations treating thermal nonequilibrium flows into SIERRA/SPARC. This new code implementation has been used to design shock-tunnel test conditions that highlight the impact of thermal nonequilibrium. This code can currently be run by experimentalists to design additional test conditions.
- Addition of these high-speed diagnostic capabilities, co-located with unique facilities such as HST, combines with Sandia capabilities for hypersonic mod-sim and flight testing to leave the Laboratories well-positioned for high-impact hypersonic work.

These impacts have been made possible through the following set of *S&T achievements*:

- Implementation of high-speed tunable laser sources (Section 3.1) that extend Sandia hypersonic diagnostics capabilities from data rates of 1 kHz to 100 kHz or higher. These new high-speed capabilities allow us to time resolve events in an impulsive test facility, such as the Sandia HST.
- Demonstration of gas-phase thermometry of the N_2 molecule in HST using the coherent anti-Stokes Raman scattering (CARS) technique. This was accomplished using picosecond burst-mode pulses for equilibrium gas thermometry in the HST shock tube (Section 0) and later improved with longer, nanosecond pulses by the first application nonlinear OPO schemes to pulse-burst pumping. This resulted in the first ever demonstration of high-speed non-equilibrium thermometry with the CARS technique (Section 3.3)
- Time-resolved planar imaging of the NO molecule at speeds up to 200 kHz using laser-induced fluorescence. This capability enables us to visualize unsteady hypersonic flow fields at high enthalpies with chemical nonequilibrium (Section 2.4), and was later applied for quantitative measurements of test facility free-stream speed.
- First-ever application of time-resolved diagnostics at the challenging, extreme temperature conditions, $T > 4000$ K, relevant to hypersonic flight (Sections 3.2–3.4).

REFERENCES

1. C. Park, "Reivew of chemical-kinetic problems of future NASA missions I: earth entries," Journal of Thermophysics and Heat Transfer **7**, 385-398 (1993).
2. C. Park, *Nonequilibrium hypersonic aerothermodynamics* (Wiley, 1990).
3. B. Thurow, N. Jiang, and W. Lempert, "Review of ultra-high repetition rate laser diagnostics for fluid dynamic measurements," Measurement Science Technology **24**, 012002 (2013).
4. M. N. Slipchenko, T. R. Meyer, and S. Roy, "Advances in burst-mode laser diagnostics for reacting and nonreacting flows," Proceedings of the Combustion Institute **38** (2021).
5. N. Jiang, W. R. Lempert, G. L. Switzer, T. R. Meyer, and J. R. Gord, "Narrow-linewidth megahertz-repetition-rate optical parametric oscillator for high-speed flow and combustion diagnostics," Applied Optics **47**, 64-71 (2008).
6. N. Jiang, P. Hsu, M. N. Slipchenko, J. F. Felver, S. Roy, J. Estevadeordal, and J. R. Gord, "A three-legged burst-mode laser system for high-speed flow and combustion diagnostics," AIAA2019-0573, AIAA SciTech Forum, San Diego, CA (2019).
7. S. Roy, P. S. Hsu, N. Jiang, M. N. Slipchenko, and J. R. Gord, "100-kHz-rate gas-phase thermometry using 100-ps pulses from a burst-mode laser," Optics Letters **40**, 5125–5128 (2015).
8. D. K. Lauriola, P. S. Hsu, N. Jiang, M. N. Slipchenko, T. R. Meyer, and S. Roy, "Burst-mode 100 kHz N_2 ps-CARS flame thermometry with concurrent nonresonant background referencing," Optics Letters **46**, 5489-5492 (2021).
9. E. R. Jans, D. J. Armstrong, A. V. Smith, and S. P. Kearney, "Noncolinear optical parametric oscillator for broadband nanosecond pulse-burst CARS diagnostics in gases," Optics Letters **47**, 1839-1842 (2022).
10. S. P. Kearney, K. A. Daniel, J. Wagner, K. P. Lynch, C. R. Downing, D. K. Lauriola, J. Leicht, and M. N. Slipchenko, "Burst-mode coherent anti-Stokes Raman scattering N_2 thermometry in the Sandia free-piston shock tube," AIAA2022-0894, AIAA SciTech Forum, San Diego, CA (2022).
11. E. R. Jans, S. P. Kearney, D. J. Armstrong, and A. V. Smith, "Demonstration of a burst-mode pumped noncolinear optical parametric oscillator (NOPO) for broadband CARS diagnostics in gases," AIAA2022-0896, AIAA SciTech Forum, San Diego, CA (2022).
12. S. P. Kearney, D. K. Lauriola, H. U. Stauffer, P. Hsu, N. Jiang, V. Athmanathan, T. R. Meyer, and S. Roy, "Analysis of picosecond coherent anti-Stokes Raman spectra for gas-phase diagnostics," Journal of the Optical Society of America B (to be ubmitted) (2022).
13. K. P. Lynch, T. W. Grasser, R. W. Spillers, C. R. Downing, K. A. Daniel, E. R. Jans, S. P. Kearney, B.J. Morreale, R. Wagnild, and J. L. Wagner, "Design and characterization of the Sandia free-piston reflected shock tunnel," Shock Waves (accepted) (2022).
14. S. P. Kearney, K. P. Lynch, K. A. Daniel, E. R. Jans, C. R. Downing, J. L. Wagner, A. M. Webb, C. Q. Crabtree, and M. N. Slipchenko, "Burst-mode laser-induced fluorescence of nitric oxide in the Sandia free-piston shock tunnel," AIAA SciTech Forum (accepted), National Harbor, MD (2023). SAND2022-7848A.
15. E. R. Jans, K. P. Lynch, K. A. Daniel, C. R. Downing, J. L. Wagner, and S. P. Kearney, "Characterization of shock-tunnel free-stream nonequilibrium using nanosecond pulse-burst coherent anti-Stokes Raman scattering," AIAA SciTech Forum (accepted), National Harbor, MD (2023). SAND2022-7070A.

16. Z. Eckert, and M. A. Gallis, "Enforcing detailed balance in the Borgnakke-Larsen redistribution method with temperature-dependent relaxation models," Physics of Fluids **34**, 066118 (2022).
17. L. Dechant, R. M. Wagnild, K. P. Lynch, S. P. Kearney, and J. L. Wagner, "High-enthalpy differential equation-based estimates for spherical/cylindrical forebody shock stand-off distance," AIAA SciTech Forum (accepted), National Harbor, MD (2023). SAND2022-7196C.
18. E. R. Jans, K. A. Daniel, C. J. Downing, K. P. Lynch, J. L. Wagner, and S. P. Kearney, "Pulse-burst N_2 CARS measurements in the non-equilibrium free stream of the Sandia free-pistion shock tunnel," AIAA SciTech Forum (accepted), National Harbor, MD (2023). SAND2022-7970A.
19. A. C. Eckbreth, *Laser Diagnostics for Combustion Temperature and Species* (Gordon and Breach, 1996).
20. P. Wu, W. R. Lempert, and R. B. Miles, "Megahertz pulse-burst laser and visualization of shock-wave/boundary-layer interaction," AIAA Journal **38**, 672-679 (2000).
21. B. Thurow, N. Jiang, and W. Lempert, "Review of ultra-high repetition rate laser diagnostics for fluid dynamic measurements," Measurement Science and Technology **24**, 012002 (2013).
22. A. C. Eckbreth, G. M. Dobbs, J. H. Stufflebeam, and P. A. Tellex, "CARS Temperature and Species Measurements in Augmented Jet Engine Exhausts," Applied Optics **23**, 1328-1339 (1984).
23. M. Aldén, and S. Wallin, "CARS Experiments in a Full-Scale (10 × 10 m) Industrial Coal Furnace," Applied Optics **24**, 3434-3437 (1985).
24. S. P. Kearney, and T. W. Grasser, "Laser-diagnostic mapping of temperature and soot statistics in a 2-m diameter turbulent pool fire," Combustion and Flame **186**, 32-44 (2017).
25. S. O'Byrne, P. M. Danehy, S. A. Tedder, and A. D. Cutler, "Dual-Pump Coherent Anti-Stokes Raman Scattering Measurements in a Supersonic Combustor," AIAA Journal **45**, 922-933 (2007).
26. M. A. Woodmansee, V. Iyer, J. C. Dutton, and R. P. Lucht, "Nonintrusive pressure and temperature measurements in an underexpanded sonic jet flowfield," AIAA Journal **42**, 1170-1180 (2004).
27. S. Roy, J. R. Gord, and A. K. Patnaik, "Recent Advances in Coherent Anti-Stokes Raman Scattering Spectroscopy: Fundamental Developments and Applications in Reacting Flows," Progress in Energy and Combustion Science **36**, 280-306 (2010).
28. R. Pan, U. Retzer, T. Werblinsski, M. N. Slipchenko, T. R. Meyer, L. Zigan, and S. Will, "Generation of high-energy, kilohertz-rate narrowband tunable ultraviolet pulses using a burst-mode dye laser system," Optics Letters **43**, 1191-1194 (2018).
29. D. K. Lauriola, P. S. Hsu, N. Jiang, M. N. Slipchenko, T. R. Meyer, and S. Roy, "Burst-mode 100-kHz N_2 ps-CARS flame thermometry with concurrent nonresonant background referencing," Optics Letters **46**, 5489-5492 (2021).
30. J. H. Frank, "Advances in imaging of chemically reacting flows," The Journal of Chemical Physics **154**, 040901 (2021).
31. L. M. L. Cantu, E. C. A. Gallo, A. D. Cutler, P. M. Danehy, C. T. Johansen, R. D. Rockwell, C. P. Goyne, and J. C. McDaniel, "OH PLIF visualization of a premixed ethylene-fueled dual-mode scramjet combustor," AIAA2016-1763, AIAA SciTech Forum, San Diego, CA (2016).
32. N. Jiang, J. Bruzzese, R. Patton, J. Sutton, R. Yentsch, D. V. Gaitonde, W. R. Lempert, J. D. Miller, T. R. Meyer, R. Parker, T. Wadham, M. Holden, and P. M. Danehy, "NO PLIF imaging in the CUBRC 48-inch shock tunnel," Experiments in Fluids **53**, 1637-1646 (2012).

33. P. S. Hsu, A. K. Patnaik, J. R. Gord, T. R. Meyer, W. D. Kulatilaka, and S. Roy, "Investigation of optical fibers for coherent anti-Stokes Raman scattering (CARS) spectroscopy in reacting flows," Experiments in Fluids **49**, 969-984 (2010).
34. T. R. Meyer, S. Roy, and J. R. Gord, "Improving signal-to-interference ratio in rich hydrocarbon-air flames using picosecond coherent anti-Stokes Raman scattering," Applied Spectroscopy **61**, 1135-1140 (2007).
35. S. P. Sharma, S. M. Ruffin, W. D. Gillespie, and S. A. Meyer, "Vibrational relaxation measurements in an expanding flow using spontaneous Raman scattering," Journal of Thermophysics and Heat Transfer **7**, 697-703 (1993).
36. P. A. de-Souza Matos, L. G. Berreta, C. A. Martins, and D. Carinhana, "Single image molecular tagging velocimetry," Measurement Science and Technology **32**, 025301 (2021).
37. P. A. de-Souza Matos, L. G. Barreta, and C. A. Martins, "Velocity and NO-Lifetime Measurements in an Unseeded Hypersonic Air Flow," Journal of Fluids Engineering **140** (2018).

APPENDIX A. MULTI VIBRATIONAL TEMPERATURE MODEL IN SIERRA/SPARC

Introduction

Sandia Parallel Aerodynamics and Reentry Code (SPARC) is a computational fluid dynamics (CFD) software for simulating aero-thermodynamics environments for atmospheric flight vehicles at various flight conditions, ranging from low-Mach transonic to high-Mach hypersonic flight conditions. SPARC is available at differing design fidelities based on the needs of applications [1]. For its highest fidelity engineering simulations, SPARC solves the compressible Navier-Stokes equations with Reynolds-Averaged Navier-Stokes (RANS) equations to model turbulent flows.

In hypersonic flows, flight vehicles are subjected to high-speed and high enthalpy environments. Under these conditions, the total energy of the flow increases due to the kinetic energy associated with high velocity or internal energy associated with high temperatures, all of which can lead to different chemical and thermal states in a flow. Changes in chemical state of the flow can occur as the molecules dissociate and exchange. There are different chemical states characterized by the relative time scales of chemical processes and the flow. Most applicable chemical state for hypersonic flows is chemical nonequilibrium where the chemical reaction time scales are comparable to the flow time scales, thus chemical rate processes cannot be neglected. As molecules are excited in high energy flows, some internal energy modes (translational, rotational, vibrational, and electronic) may no longer be assumed in equilibrium due to the short time scales. The collisional characteristic time for translational and rotational modes are relatively fast. Therefore, for hypersonic flows, vibrational modes become an important aspect to model as the characteristic time scale is comparable to the flow time [6].

To model these flow conditions in thermo-chemical nonequilibrium states, the governing equations, conservations of mass, momentum, and energy, are solved with additional models that describe the chemistry and thermodynamic changes. Currently in SPARC, the thermochemical nonequilibrium flow is modeled by the 5, 7, or 11 species reacting gas finite-rate chemistry model with the thermally perfect gas equation of state to describe nonequilibrium internal energies in translational, rotational, and vibrational mode. These models are fully coupled with the compressible Navier-Stokes RANS equations for the nonequilibrium thermochemical simulations in hypersonic flow conditions. As part of the LDRD project, we have developed the multi-vibrational temperature model. The multi-vibrational temperature model aims to treat each diatomic vibrational species separately, thus allowing for the modeling of the vibrational energy transfer from one species to the other vibrationally excited species. Because of this, unlike the standard two-temperature model where only one vibrational temperature is used, the new model can lead to modeling and prediction of each vibrational species temperature with higher degree of fidelity. This model can especially be beneficial in diagnostics of hypersonic flows or high-altitude flight vehicles in which higher-degrees of thermochemical nonequilibrium can cause each vibrational mode to have different relaxation characteristics.

Governing Equations

The governing equations for thermochemical nonequilibrium flows can be expressed as follows

$$\frac{d\mathbf{U}}{dt} + \nabla \cdot \mathbf{F}^I = \nabla \cdot \mathbf{F}^V + \mathbf{W}. \tag{1}$$

The conserved vector $\mathbf{U}$ is

$$\mathbf{U} = (\rho_s, \rho u, \rho v, \rho w, \rho E_t, \rho_s e_{v,m})^T \tag{2}$$

where subscript $\mathbf{s}$ corresponds to species and $\boldsymbol{\rho_s e_{v,m}}$ is the vibrational energy for vibrational mode $\mathbf{m}$ for a diatomic species $\mathbf{s}$. The total energy is defined as

$$\rho E_t = \sum_s \rho_s C v_s T + \sum_s \rho_s e_{v,m} + \frac{1}{2}\sum_s \rho_s (u_j u_j) + \sum_s \rho_s h_{0,s} \tag{3}$$

where $\mathbf{C}\boldsymbol{v_s}$ is the volume-constant specific heat for species $\mathbf{s}$, and $\boldsymbol{h_{0,s}}$ is the heat of formation. A common assumption that the rotational energy mode equilibrates quickly is made, thus, the rotational and translational energy modes are modeled as one translational temperature. The vibrational energy is defined as a simple harmonic oscillator model

$$e_{v,m} = R_m \frac{\theta_{v,m}}{\exp\left(\theta_{v,m}/T_{v,m}\right) - 1} \tag{4}$$

where $\mathbf{R_m}$ is the gas constant for diatomic species corresponding to vibrational mode $\mathbf{m}$, the $\boldsymbol{\theta_{v,m}}$ is the characteristic temperature of vibration.

The inviscid flux vector is expressed as follows

$$\mathbf{F}_i^I = \begin{pmatrix} \rho_s u_i \\ \rho u u_i + \delta_{i1} p \\ \rho v u_i + \delta_{i2} p \\ \rho w u_i + \delta_{i3} p \\ \rho u_i H \\ \rho_s u_i e_{v,m} \end{pmatrix} \tag{5}$$

where $\boldsymbol{H = E_t + \frac{p}{\rho}}$ is the enthalpy. In the single vibrational temperature model, Eq. (5), the vibrational energy flux component is the sum of all available vibrational energy modes, $\boldsymbol{\rho u_i e_v = \sum_s \rho_s u_i e_{v,m}}$. In contrast, each diatomic vibrational energy mode is a separate degree of freedom in the multi-vibrational temperature model.

The viscous flux vector is

$$\mathbf{F}_i^V = \begin{pmatrix} \rho_s v_{si} \\ \tau_{ix} \\ \tau_{iy} \\ \tau_{iz} \\ \tau_{ij} u_j - ((q_t)_i + \sum_s (q_{v,m})_i + \sum_s \rho_s v_{si} h_s) \\ -(q_{v,m})_i - \sum_s \rho_s v_{si} e_{v,m} \end{pmatrix} \tag{6}$$

where $\rho_s v_{si}$ is the species diffusion flux, τ_{ij} is the viscous stress tensor, q_t and q_v are the heat flux for translational and vibrational energy mode, respectively. The species diffusion flux is assumed to be only driven by species gradients and is modeled by the modified Fick's law with a constant effective diffusion coefficient,

$$\rho_s v_{si} = \mathcal{D}_s \frac{\partial \rho_s}{\partial x_i} = -\rho \mathcal{D}_s \frac{\partial c_s}{\partial x_i} \tag{7}$$

where $\mathcal{D}_s$ is the effective diffusion coefficient and c_s is the mass fraction of species s. The effective diffusion coefficient is defined as

$$\mathcal{D}_s = \frac{Le\, \kappa_s}{\rho_s C p_s} \tag{8}$$

and the assumption is made with a constant Lewis number, $Le = 1.4$. The viscous stress tensor is

$$\tau_{ij} = \mu \left(\frac{\partial u_i}{\partial x_j} + \frac{\partial u_j}{\partial x_i} \right) - \frac{2}{3} \mu \frac{\partial u_k}{\partial x_k} \delta_{ij} \tag{9}$$

where μ is the viscosity.

The translational and vibrational heat flux are expressed as

$$(q_t)_j = -\sum_s \kappa_s \frac{\partial T}{\partial x_j} \tag{10}$$

$$(q_{v,m})_j = -\kappa_{v,m} \frac{\partial T_{v,m}}{\partial x_j} \tag{11}$$

where κ is the thermal conductivity of species s.

The source term vector is

$$\mathbf{W} = (\dot{\omega}_s, 0, 0, 0, 0, S_{v,m})^T \tag{12}$$

where $\dot{\omega}_s$ is the species mass production rates of chemical reactions and $S_{v,m}$ is the vibrational energy source term [2].

The species mass production rates of chemical reactions term $\dot{\omega}_s$ describes the rate at which species are produced or destroyed in each reaction set. The chemical source term is expressed in the following general form

$$\dot{\omega}_s = M_s \sum_r (\alpha_{sr} - \beta_{sr}) \mathcal{R}_r \tag{13}$$

where M_s is the molecular mass, α_{sr} is the stoichiometric coefficient of the reactant species s for reaction r, β_{sr} is the stoichiometric coefficient of the product species s for reaction r, and $\mathcal{R}_r$ is the reaction rate [3]. The reaction rate is the difference between the forward and backward reaction rates

$$\mathcal{R}_r = \mathcal{R}_{b,r} - \mathcal{R}_{f,r} = k_{b,r} \prod_s \left(\frac{\rho_s}{M_s}\right)^{\beta_{sr}} - k_{f,r} \prod_s \left(\frac{\rho_s}{M_s}\right)^{\alpha_{sr}} \tag{14}$$

where $k_{f,r}$ and $k_{b,r}$ are the forward and backward rate coefficients. These rate coefficients are determined experimentally and have the following form

$$k_{f,r} = C_{f,r} \exp\left(\eta_r \ln T_{\text{eff}} - \theta_r / T_{\text{eff}}\right), \quad k_{b,r} = \frac{k_{f,r}}{K_{eq,r}} \tag{15}$$

where T_{eff} is the effective temperature, $C_{f,r}$ is the reaction rate constant, η_r is the Arrhenius pre-exponent factor, θ_r is the activation energy, and $K_{eq,r}$ is the equilibrium constant for reaction r [2,6]. The effective temperature is a function of internal energy temperatures. For the case of vibrational nonequilibrium, the geometric mean of the translational-rotational and the vibrational temperature, $T_{\text{eff}} = \sqrt{T T_{v,m}}$, is used as the effective temperature [2,7].

The 5 species air model [4] is used for the multi-vibrational temperature model. The model consists of N_2, O_2, NO, N, and O species, and there are 5 reactions.

$$\begin{aligned}
N_2 + \mathcal{M} &\leftrightharpoons 2N + \mathcal{M} && (\mathrm{r} = 1, \text{dissociation}) \\
O_2 + \mathcal{M} &\leftrightharpoons 2O + \mathcal{M} && (\mathrm{r} = 2, \text{dissociation}) \\
NO + \mathcal{M} &\leftrightharpoons N + O + \mathcal{M} && (\mathrm{r} = 3, \text{dissociation}) \\
N_2 + O &\leftrightharpoons NO + N && (\mathrm{r} = 4, \text{exchange}) \\
NO + O &\leftrightharpoons O_2 + N && (\mathrm{r} = 5, \text{exchange})
\end{aligned} \tag{16}$$

where $\mathcal{M}$ is a collision partner, which may be any of the species. After following the preceding development, the species source terms Eq. (13) for the 5 species model are

$$\begin{aligned}
\dot{\omega}_{N_2} &= M_{N_2} (\mathcal{R}_1 + \mathcal{R}_2) \\
\dot{\omega}_{O_2} &= M_{O_2} (\mathcal{R}_2 - \mathcal{R}_5) \\
\dot{\omega}_{NO} &= M_{NO} (\mathcal{R}_3 - \mathcal{R}_4 + \mathcal{R}_5) \\
\dot{\omega}_{N} &= M_{N} (-2\mathcal{R}_1 - \mathcal{R}_3 - \mathcal{R}_4 - \mathcal{R}_5) \\
\dot{\omega}_{O} &= M_{O} (-2\mathcal{R}_2 - \mathcal{R}_3 + \mathcal{R}_4 + \mathcal{R}_5).
\end{aligned} \tag{17}$$

The vibrational energy source term [5] for species s can be further broken into the following components

$$S_{v,m} = S_{v-chem} + S_{v-trans} + S_{v-v} + S_{v-elec} \tag{18}$$

where S_{v-chem} is the vibrational energy source from chemical reactions, $S_{v-trans}$ is the vibrational-translational energy relaxation, S_{v-v} is the vibrational energy relaxation between vibrational energies of other molecules, and S_{v-elec} is the vibrational-electron energy relaxation.

The vibrational energy source from chemical reactions is

$$S_{v-chem} = \sum_s \dot{\omega}_s e_{v,m} \tag{19}$$

where the vibrational energy mode, $e_{v,m}$, is described in Eq. (4).

The vibrational translational energy relaxation term is

$$S_{v-trans} = \sum_s \rho_s \frac{e^*_{v,m}(T) - e_{v,m}(T_{v,m})}{< \tau_s >} \tag{20}$$

where $< \tau_s >$ is the vibrational-translational relaxation time and $e^*_{v,m}$ is the equilibrium vibrational energy. This mechanism describes the rate of energy exchange between the translational and vibrational energy mode.

The vibrational electron energy relaxation term is

$$S_{v-elec,s} = \rho_s \frac{e_{v,m}(T_{v,m}) - e^*_{v,m}(T_e)}{\tau_{es}} \tag{21}$$

where τ_{es} is the relaxation time. This term describes the rate of energy exchange between electron-translational and vibrational mode. In SPARC, the vibrational-electron energy relaxation is not considered.

The vibrational energy relaxation term describes the transfer of vibrational energy from one vibrational species to the other species, and is expressed as follows

$$S_{v-v} = \sum_{r \neq m} \rho_{s-m} \frac{e_{v,m}(T'_{v,m-r}) - e_{v,m}(T_{v,m})}{\tau_{vv,m-r}} \tag{22}$$

where $T'_{v,m-r}$ is the vibrational temperature after the collision between r and m diatomic molecules and $\tau_{vv,m-r}$ is the corresponding vibrational-vibrational energy relaxation time. Here, $\rho_{s-m} = \rho_s$ is employed to make a distinction that the species density s for vibrational mode m in the subsequent description. The post-collision vibrational temperature is obtained by solving the energy conservation statement before and after the collision

$$\rho_{s-m} e_{v,m}(T'_{v,m-r}) + \rho_{s-r} e_{v,r}(T'_{v,m-r}) = \rho_{s-m} e_{v,m}(T_{v,m}) + \rho_{s-r} e_{v,r}(T_{v,r}) \tag{23}$$

where ρ_{s-m} and ρ_{s-r} correspond to the species density for vibrational mode m and r. This equation is solved by iterating with the Newton-Raphson method until $T'_{v,m-r}$ is converged within a prescribed tolerance. Lastly, the vibrational-vibrational energy relaxation time is given by

$$\tau_{vv,s-r} = \frac{n_s}{P_{s,r} Z_{s,r}} \tag{24}$$

where n_s is the number density of species s, $P_{s,r}$ is the collision probability, and $Z_{s,r}$ is the collision number. An empirical expression for this relaxation time will instead be used

$$\tau_{vv,s-r} = \frac{101324}{p_s}(AT^B + C) \tag{25}$$

where p_s is the partial pressure of species s and coefficients A, B, and C for vibrational-vibrational collision for 5 species air are shown in Table 1. This form of the vibrational energy relaxation term is easily extended to other reacting gas chemistry models upon the acquisition of appropriate vibrational-vibrational energy relaxation coefficients.

Table A1: Coefficients of the vibrational-vibrational energy relaxation time

Collision	A	B	C
N_2 - NO	5.988e+5	-1.82	5.91e-13
N_2 - O_2	4.979e+5	-2.37	1.50e-13
O_2 - NO	6.191e+5	-1.82	8.31e-13

References for Appendix A

[1] *Sandia Parallel Aerodynamics Reentry Code (SPARC) – the Future of Production and Research Aerodnyamics*. SAND2020-8483R

[2] Candler G., MacCormack R., *Computation of Weakly Ionized Hypersonic Flows in Thermochemical Nonequilibrium*. J. Thermodynamics 1988.

[3] Dinzl D., Howard M., Wagnild R., Bova S., Fisher T., *Sandia Parallel Aerodynamics and Reentry Code (SPARC) Theory Manual*. SAND2016-8483.

[4] Park C., *Assessment of Two-Temperature Kinetic Model for Ionizing Air*. AIAA Paper 87-1574, June 1987.

[5] Kim M., Koch U., Esser B., Gulhan A., *Numerical and Experimental Study of High Enthalpy Flows in a Hypersonic Plasma Wind Tunnel: L3K*. AIAA 2011.

[6] Vincenti W., Kruger C., *Introduction to Physical Gas Dynamics*. Krieger Publishing Company 1965.

[7] Park C., *Nonequilibrium Hypersonic Aerothermodyanmics*. Wiley 1990.

DISTRIBUTION

Email—Internal

Name	Org.	Sandia Email Address
J.S. Lash	1500	jslash@sandia.gov
J.L. Payne	1510	jlpayne@sandia.gov
C.R. Downing	1512	crdowni@sandia.gov
A.M. Grillet	1512	amgrill@sandia.gov
D.R. Guildenbecher	1512	drguild@sandia.gov
B.R. Halls	1512	brhalls@sandia.gov
E.R. Jans	1512	erjans@sandia.gov
M.D. Koll	1512	mkoll@sandia.gov
D.R. Richardson	1512	drrich@sandia.gov
W.E. Swain	1512	weswain@sandia.gov
M.D. Koll	1512	mkoll@sandia.gov
L. Collins	1513	lcolli@sandia.gov
Z. Echo	1513	zeckert@sandia.gov
R.P. Manginell	1513	rpmangi@sandia.gov
L.M. Phinney	1514	lmphinn@sandia.gov
R.B. Bhakta	1515	rbhakta@sandia.gov
S.J. Beresh	1515	sjberes@sandia.gov
K.L. Casper	1515	kmcaspe@sandia.gov
K.A. Daniel	1515	kadani@sandia.gov
L.J. Dechant	1515	ljdecha@sandia.gov
J.W. Hargis	1515	jwhargi@sandia.gov
K.P. Lynch	1515	klynch@sandia.gov
A. Pandey	1515	apandey@sandia.gov
J. Smith	1515	jussmit@sandia.gov
J.L. Wagner	1515	jwagner@sandia.gov
R.M. Wagnild	1515	rmwagni@sandia.gov
J.B. Lechman	1516	jblechm@sandia.gov
J. Engerer	1532	jengere@sandia.gov
J.B. Maeng	1541	jmaeng@sandia.gov
J. Blecke	1550	jblecke@sandia.gov
D.J. Armstrong	1682	darmstr@sandia.gov

Name	Org.	Sandia Email Address
C.M. Murzyn	6751	cmurzyn@sandia.gov
C.B. Saltonstall	6751	cbsalto@sandia.gov
R.K. Harrison	6753	rkharri@sandia.gov
E.E. Mussoni	8751	eemusso@sandia.gov
LDRD office	1910	ldrd@sandia.gov
Technical Library	1911	sanddocs@sandia.gov

Sandia National Laboratories

Sandia National Laboratories is a multimission laboratory managed and operated by National Technology & Engineering Solutions of Sandia LLC, a wholly owned subsidiary of Honeywell International Inc. for the U.S. Department of Energy's National Nuclear Security Administration under contract DE-NA0003525.